

## Original Article

**Cite this article:** Sabino M, Dela Pierre F, Natalicchio M, Birgel D, Gier S, and Peckmann J. The response of water column and sedimentary environments to the advent of the Messinian salinity crisis: insights from an onshore deep-water section (Govone, NW Italy). *Geological Magazine* <https://doi.org/10.1017/S0016756820000874>

Received: 17 February 2020

Revised: 5 June 2020

Accepted: 13 July 2020


**Keywords:**

water-column stratification; marine conditions; archaeol; GDGTs; lycopane; oxygen depletion; redox zonation

**Author for correspondence:** Jörn Peckmann,

Email: [joern.peckmann@uni-hamburg.de](mailto:joern.peckmann@uni-hamburg.de)

# The response of water column and sedimentary environments to the advent of the Messinian salinity crisis: insights from an onshore deep-water section (Govone, NW Italy)

Mathia Sabino<sup>1</sup>, Francesco Dela Pierre<sup>2</sup>, Marcello Natalicchio<sup>2</sup>, Daniel Birgel<sup>1</sup>, Susanne Gier<sup>3</sup> and Jörn Peckmann<sup>1</sup> 

<sup>1</sup>Institut für Geologie, Centrum für Erdsystemforschung und Nachhaltigkeit, Universität Hamburg, D-20146 Hamburg, Germany; <sup>2</sup>Dipartimento di Scienze della Terra, Università degli Studi di Torino, I-10125 Torino, Italy and <sup>3</sup>Department für Geodynamik und Sedimentologie, Universität Wien, A-1090 Wien, Austria

**Abstract**

During Messinian time, the Mediterranean underwent hydrological modifications culminating 5.97 Ma ago with the Messinian salinity crisis (MSC). Evaporite deposition and alleged annihilation of most marine eukaryotes were taken as evidence of the establishment of basin-wide hypersalinity followed by desiccation. However, the palaeoenvironmental conditions during the MSC are still a matter of debate, chiefly because most of its sedimentary record is buried below the abyssal plains of the present-day Mediterranean Sea. To shed light on environmental change at the advent and during the early phase of the MSC, we investigated the Govone section from the Piedmont Basin (NW Italy) using a multidisciplinary approach (organic geochemical, petrographic, and carbon and oxygen stable isotope analyses). The Govone section archives the onset of the crisis in a succession of organic-rich shales and dolomite-rich marls. The MSC part of the succession represents the deep-water equivalent of sulphate evaporites deposited at the basin margins during the first phase of the crisis. Our study reveals that the onset of the MSC was marked by the intensification of water-column stratification, rather than the establishment of widespread hypersaline conditions. A chemocline divided the water column into an oxygen-depleted, denser and more saline bottom layer and an oxygenated, upper seawater layer influenced by freshwater inflow. Vertical oscillations of the chemocline controlled the stratigraphic architecture of the sediments pertaining to the first stage of the MSC. Accordingly, temporal and spatial changes of water masses with different redox chemistries must be considered when interpreting the MSC event.

**1. Introduction**

During Messinian time (7.25–5.33 Ma) the Mediterranean area underwent progressive environmental and hydrological changes, which culminated c. 5.97 Ma ago with the Messinian salinity crisis (MSC; Hsü *et al.* 1973; Roveri *et al.* 2014; Camerlenghi & Aloisi, 2020). During this event, the Mediterranean Sea turned into the youngest Salt Giant of Earth history (Warren, 2010) as a response of its isolation from the global ocean caused by the restriction of the Mediterranean–Atlantic gateways (Flecker *et al.* 2015; Krijgsman *et al.* 2018; Capella *et al.* 2019). One of the most striking effects of the hydrological changes that affected the basin was the intensification of water-column stratification and consequent development of bottom-water anoxia starting at c. 6.7 Ma (Roveri *et al.* 2014). The deterioration of palaeoenvironmental conditions was recorded by the deposition of precession-paced alternations of organic-rich shales, diatomites and marls (Hilgen & Krijgsman, 1999; Sierro *et al.* 1999; Krijgsman *et al.* 2002). Starting from 5.97 Ma (Manzi *et al.* 2013), the shale-diatomite-marl successions were replaced at the basin margins by couplets of sulphate evaporites and organic-rich shales of the Primary Lower Gypsum unit (PLG; Roveri *et al.* 2008), marking the first stage of the MSC (5.97–5.60 Ma; Roveri *et al.* 2014). The deposition of evaporites has been considered as compelling evidence of the development of hypersaline conditions, which resulted in the demise of most marine eukaryotes (e.g. Bellanca *et al.* 2001), but promoted the rise of halophilic prokaryotes (Turich & Freeman, 2011; Birgel *et al.* 2014). The PLG unit passes laterally in intermediate-to deep-water settings (> 200 m depth) into evaporite-free successions, composed of shales alternating with carbonates and/or dolomite-rich marls barren of calcareous microfossils (Manzi *et al.* 2007, 2011; Dela Pierre *et al.* 2011; Roveri *et al.* 2014; Natalicchio *et al.* 2019).

After the formulation of the ‘deep desiccated basin model’ in the 1970s (Hsü *et al.* 1973), the palaeoenvironmental conditions of the Mediterranean water column and seafloor during the MSC are still a matter of debate. The scarcity or lack of body fossils in MSC sediments, the lack

of modern analogues for the Messinian evaporites and the inaccessibility of the offshore evaporites have hampered the development of a widely accepted scenario (Rouchy & Caruso, 2006; Ryan, 2009; Roveri *et al.* 2014; Camerlenghi & Aloisi, 2020).

The analysis of molecular fossils (lipid biomarkers) preserved in Messinian evaporites and their intermediate- to deep-water lateral equivalents provides fundamental information for the reconstruction of the Mediterranean hydrological cycle and palaeoenvironments (Vasiliev *et al.* 2017; Natalicchio *et al.* 2019; Sabino *et al.* 2020). This approach is a valuable tool to unveil the conditions in the water column during the MSC. Organic geochemical investigations targeting abyssal evaporites (Christeleit *et al.* 2015) and Messinian salts (Isaji *et al.* 2019b) revealed that evaporites were deposited under a stratified water column during the latest MSC phases. These results agree with recent hydrological models (de Lange & Krijgsman, 2010; Simon & Meijer, 2017; García-Veigas *et al.* 2018). In contrast, only a few geochemical data are available for the sediments deposited during the early stages of the MSC (Kenig *et al.* 1995; Sinninghe Damsté *et al.* 1995b; Isaji *et al.* 2019a). These studies all describe organic-rich shales of the PLG unit, depicting a stratified basin that received freshwater from rivers (Natalicchio *et al.* 2017, 2019; Sabino *et al.* 2020) and/or low-salinity water from the Paratethys (Grothe *et al.* 2020).

To shed new light on the response of the water column and sediments to the advent of the MSC, we studied sedimentary strata exposed in the Govone section (Piedmont Basin, NW Italy). In this section, the onset of the crisis is archived in a sequence of organic-rich shales and marls, representing the deep-water equivalents of primary sulphate evaporites deposited at the basin margins (Gennari *et al.* 2020; Sabino *et al.* 2020). These sediments have recently been investigated to reconstruct the palaeoclimate and palaeohydrologic variability in the northern Mediterranean across the onset of the MSC (Sabino *et al.* 2020). This previous study, which was based on inorganic geochemical proxies and on carbon and hydrogen stable isotope composition of lipids from terrestrial plant waxes, revealed fluctuations between more humid (shales) and more arid (marls) climates and an evolution towards moister conditions after the onset of the MSC (Sabino *et al.* 2020).

Here, we focus on the same succession studied by Sabino *et al.* (2020), integrating stratigraphic, petrographic, carbon and oxygen stable isotope analyses, and the study of molecular fossils to reconstruct the palaeoenvironments. This approach allows us to reconstruct the environmental changes across the onset of the MSC, and reveals how these changes influenced the stratigraphic architecture of the sediments deposited during times of change in the Mediterranean realm.

## 2. Geological setting

### 2.a. The Messinian succession in the Piedmont Basin

The Piedmont Basin (NW Italy; Fig. 1a) is a wedge-top basin located on the inner side of the SW Alpine arc filled with upper Eocene – Messinian sediments (Rossi *et al.* 2009; Mosca *et al.* 2010). The Messinian succession is exposed on the uplifted southern and northern margins of the basin and starts with outer shelf to slope marls and shales (Sant'Agata Fossili Marls; Tortonian – lower Messinian; Sturani & Sampò, 1973). These deposits, characterized by the repetition of shale and marl couplets, record progressively more restricted conditions heralding the onset of the MSC (Sturani, 1973; Sturani & Sampò, 1973). The lithological cyclicity was controlled by climate fluctuations driven by

precession, with shales representing more humid conditions at precession minima and marls recording more arid conditions at precession maxima (Natalicchio *et al.* 2019; Sabino *et al.* 2020). At the basin margins, this unit is overlain by shale and gypsum couplets belonging to the PLG unit (Fig. 1b). In settings of intermediate water depth, the gypsum beds of the lowermost PLG cycles are transitional to carbonate-rich layers and marls hosting fossilized microbial mats of putative sulphide-oxidizing bacteria, in turn passing in deep-water settings into dolomite-rich marls (Dela Pierre *et al.* 2012, 2016; Natalicchio *et al.* 2017, 2019; Sabino *et al.* 2020; Fig. 1c). In the basin depocentre, only shales and marls are found (Irace *et al.* 2009). The PLG unit and its deeper-water equivalents are overlain by chaotic and clastic gypsum facies (Valle Versa Chaotic complex; Irace *et al.* 2005; Dela Pierre *et al.* 2007), which are correlated to the Resedimented Lower Gypsum unit deposited during the second stage of the MSC (5.60–5.55 Ma; Roveri *et al.* 2014). The Messinian succession is completed by fluvio-deltaic and lacustrine sediments, referred to as the Cassano Spinola Conglomerates (Sturani, 1976; Dela Pierre *et al.* 2011, 2016; Fig. 1c), recording the third stage of the MSC (5.55–5.33 Ma; Roveri *et al.* 2014).

### 2.b. The Govone section and the position of the MSC onset

In the Govone section, located at the southern margin of the Piedmont Basin (44° 48' 08" N; 8° 07' 34" E; Fig. 1b), the whole Messinian succession is exposed, starting with 35 lithologic cycles up to 2 m in thickness (Gm1–Gm35; Bernardi *et al.* 2012; Bernardi, 2013; Dela Pierre *et al.* 2016; Gennari *et al.* 2020; Sabino *et al.* 2020; Fig. 2). These cycles consist of shale/marl couplets and belong to the Sant'Agata Fossili Marls. This unit is conformably overlain by the PLG unit (Fig. 1c), made up of nine cycles (Gg1–Gg9) of shales and gypsum-rich layers; the latter consist of flattened conical structures formed by millimetre-sized gypsum crystals enclosed in laminated gypsiferous silty mudstones (Bernardi, 2013). The PLG is in turn overlain by shales and clastic evaporites belonging to the Valle Versa Chaotic complex, finally followed by fluvio-deltaic deposits of the Cassano Spinola Conglomerates (Fig. 1c; Bernardi, 2013; Dela Pierre *et al.* 2016; Sabino *et al.* 2020).

The age model for the Govone section (Gennari *et al.* 2020) had already been adopted by Sabino *et al.* (2020). The position of the MSC onset (5.97 Ma; Manzi *et al.* 2013) was defined through the identification of diagnostic planktonic foraminifer bioevents, the ages of which were calibrated through the correlation with the astronomically tuned Perales section (Sierro *et al.* 2001, 2003; Manzi *et al.* 2013; Fig. 2). The main bioevents identified by Gennari *et al.* (2020) are: (1) the first abundant occurrence (FAO) of *Turborotalita multiloba* in cycle Gm12, occurring in cycle UA15 in Perales and dated 6.415 Ma (Sierro *et al.* 2001); (2) the left/right coiling change of *Neogloboquadrina acostaensis* in cycle Gm14, identified in Perales at cycle UA17 and dated 6.36 Ma (Sierro *et al.* 2001); (3) the first influx of *Globorotalia scitula* in cycle Gm17, dated 6.29 Ma in the Perales section (cycle UA20; Sierro *et al.* 2001); and (4) a second influx of *Globorotalia scitula* in cycle Gm24, which falls within an acme interval of *T. multiloba*. For the Perales section, Sierro *et al.* (2001) reported this acme between cycles UA23 and UA30, allowing Gennari *et al.* (2020) to correlate the second influx of *G. scitula* in the Govone section with the second influx recognized in cycle UA29 in the Perales section and dated at 6.10 Ma. Since the second influx of *G. scitula* occurs six precession cycles below the onset of the crisis in the Perales section (Sierro *et al.* 2001), the MSC onset in Govone was placed at the base

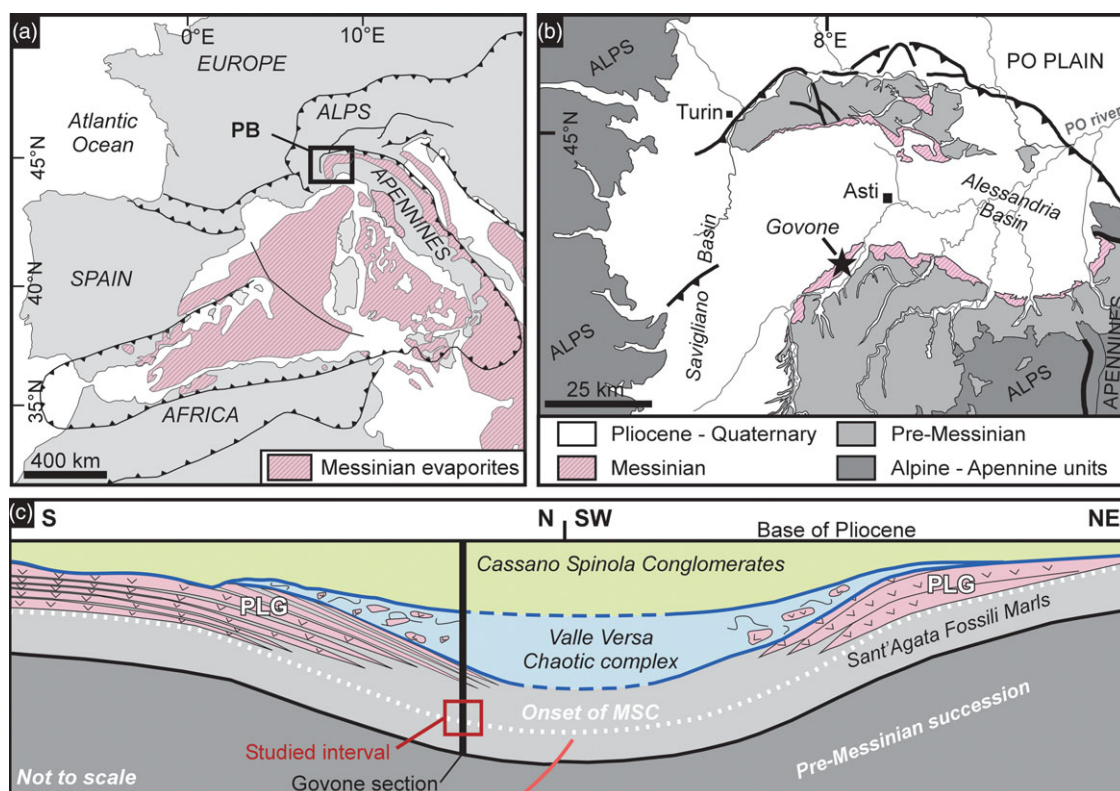


**Fig. 1.** (Colour online) (a) Distribution of the Messinian evaporites (pink) in the Western Mediterranean Basin and location of the Piedmont Basin (black box; modified from Manzi *et al.* 2013). (b) Structural sketch map of the Piedmont Basin (modified from Bigi *et al.* 1990); the star indicates the location of the Govone section. (c) Schematic profile of the Piedmont Basin, showing the stratigraphic architecture of the Messinian succession; the Govone section (vertical black bar) and the studied interval (red box) are indicated. Note that the gypsum beds are progressively younger towards the depocentre. MSC – Messinian salinity crisis; PB – Piedmont Basin; PLG – Primary Lower Gypsum (modified from Dela Pierre *et al.* 2011).

of the marls of cycle Gm30 (Gennari *et al.* 2020; Sabino *et al.* 2020; Fig. 2), which accordingly correspond to the gypsum bed in cycle PLG1 of Perales (Fig. 2; Manzi *et al.* 2013).

According to the adopted model, the uppermost six Sant'Agata Fossili Marls cycles below the first local gypsum bed (Gg1 cycle) represent the deep-water counterparts of the lowermost PLG cycles (Fig. 2), with marls representing the time equivalents of the shallow-water marginal gypsum (Gennari *et al.* 2020; Sabino *et al.* 2020). In this study we investigate four pre-MS (Gm26–Gm29) and four MSC (Gm30–Gm33) cycles, representing a time interval of *c.* 150 ka. Younger strata of the Govone section containing gypsum (Fig. 1c) are not studied here.

### 3. Materials and methods

#### 3.a. Petrography and mineralogy

A total of 33 fresh, unweathered samples were excavated from cycles Gm26 to Gm33 (on average, 4 samples per cycle); the Govone sedimentary rocks tend to be well preserved and continuously exposed due to ongoing erosion in the river bed. A total of 18 slabs and thin-sections were obtained from representative samples (10 from pre-MS cycles and 8 from MSC cycles) and studied at the Department of Earth Sciences, University of Turin by optical (transmitted, reflected and UV light) and scanning electron microscopy (SEM). SEM analyses were performed on carbon-coated stubs for morphological analyses and on carbon-coated, polished thin-sections for semi-quantitative elemental analysis and backscattered electron imagery, using a JEOL JSM IT300LV

scanning electron microscope equipped with an energy-dispersive EDS Oxford Instrument Link System microprobe (University of Turin).

X-ray diffraction (XRD) analyses were performed on all 33 samples using a Panalytical X'Pert PRO diffractometer (CuK $\alpha$  radiation, 40 kV, 40 mA, step size 0.0167, 5 s per step) at the Department of Geodynamics and Sedimentology, University of Vienna. The samples were loaded in the sample holders as oriented powders. The X-ray diffraction patterns were interpreted using the Panalytical software 'X'Pert High score plus' to determine the carbonate phase mineralogy.

#### 3.b. Carbon and oxygen stable isotopes

Carbon ( $\delta^{13}\text{C}$ ) and oxygen ( $\delta^{18}\text{O}$ ) bulk-rock stable isotope analyses were performed on 9 samples (pre-MS cycles, 1 sample; MSC cycles, 8 samples). These analyses add to those of Bernardi (2013) who analysed 20 samples, 12 from pre-MS cycles and 8 from MSC cycles. Analyses were performed at the MARUM stable isotope laboratory (University of Bremen). The 9 new samples were measured at 75°C on a Finnigan MAT 252 gas isotope ratio mass spectrometer connected to a Kiel III automated carbonate preparation device. The instrument was calibrated against an in-house standard (ground Solnhofen limestone), which in turn was calibrated against the NBS 19 calcite standard. Over the measurement period, the standard deviations of the in-house standard were 0.04‰ for  $\delta^{13}\text{C}$  and 0.06‰ for  $\delta^{18}\text{O}$  values. Data are reported in delta-notation versus V-PDB. When dolomite was the only carbonate phase, the  $\delta^{18}\text{O}$  values were corrected for  $-0.8\text{‰}$  for



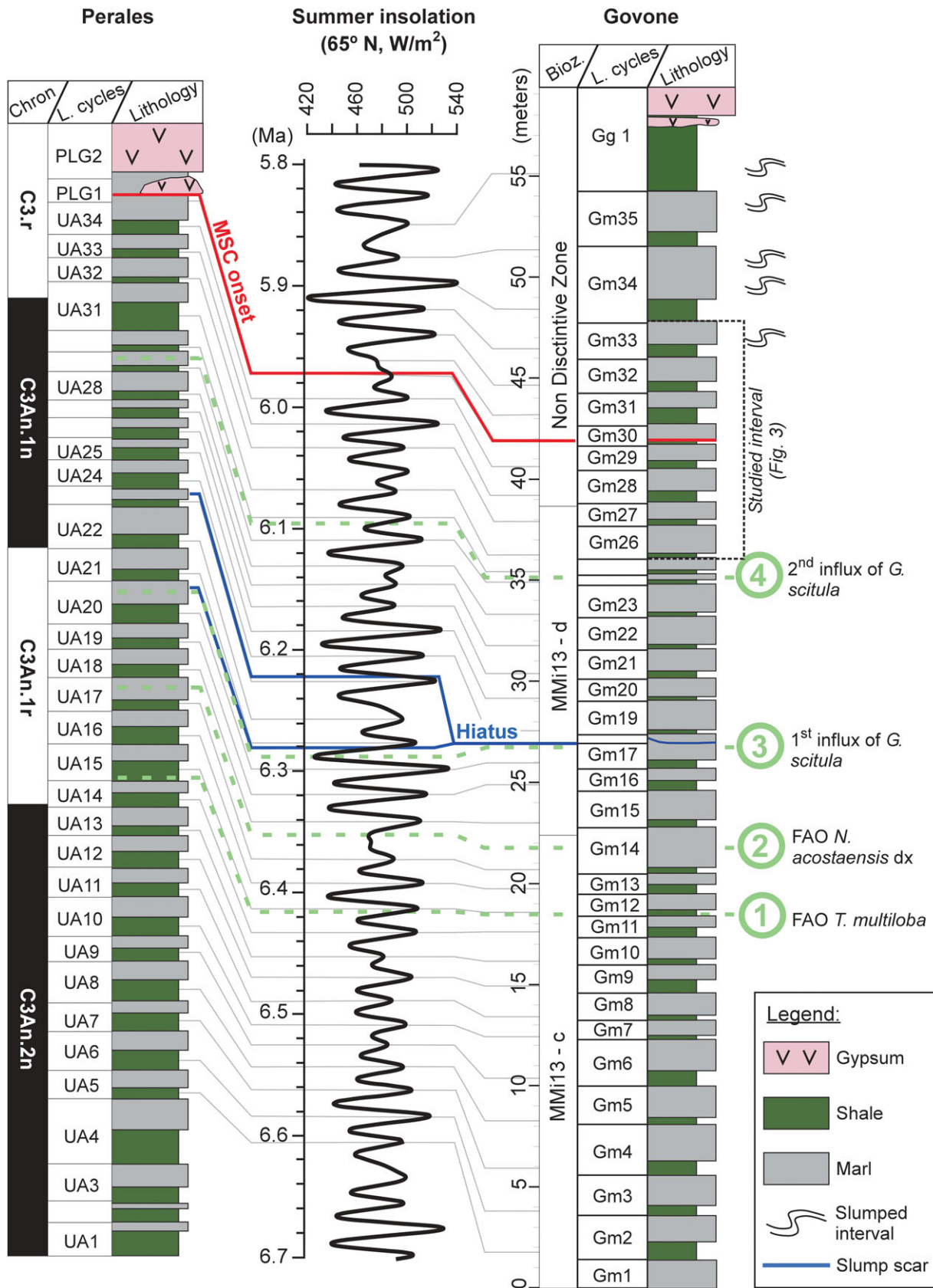


**Fig. 2.** (Colour online) Tuning of the Govone section with the astronomical solution (65° N summer insolation; Laskar *et al.* 2004) and correlation with the Perales section (Spain; Sierra *et al.* 2001; Manzi *et al.* 2013). Numbers in circles on the right represent the main bioevents reported in the main text. Bioz. – biozones; FAO – first abundant occurrence (modified from Gennari *et al.* 2020; Sabino *et al.* 2020).

measurements from Bernardi (2013; analyses performed at 50°C; Sharma & Clayton, 1965) and  $-1.2\%$  for the new measurements (analyses performed at 75°C; Rosenbaum & Sheppard, 1986; Kim *et al.* 2007). The correction was necessary to account for the fractionation effect during the phosphoric acid reaction (see online Supplementary Material, available at <http://journals.cambridge.org/geo>, for further details).

### 3.c. Total inorganic and organic carbon contents

Total inorganic (TIC) and organic (TOC) carbon contents were measured at the Institute for Geology of the University of Hamburg. After drying (at 50°C for 24 h), the samples were manually ground with an agate mortar. The powders were split in two aliquots: one fraction was heated to 1350°C and total carbon (TC) contents were measured using a LECO SC-144DR Carbon Analyser equipped with an infrared detector. The second fraction was first heated to 550°C for 5 h to remove organic carbon (OC) and then heated to 1350°C to measure TIC contents. Prior to and after sample analyses, a Synthetic Carbon Leco 502-029 ( $1.01 \pm 0.02$  carbon%) standard was measured. TOC contents were determined using the formula  $TOC = TC - TIC$ .

### 3.d. Lipid biomarker analyses

Lipid biomarker analyses were performed on 21 samples (at least 2 samples per cycle) using the procedure described in Sabino *et al.* (2020). Briefly, after a modified Bligh and Dyer extraction, samples were separated in an *n*-hexane-soluble and a dichloromethane-soluble fraction. The former was further separated into four sub-fractions: (a) hydrocarbons, (b) ketones, (c) alcohols and (d) carboxylic acids. The alcohol fraction was derivatized for 1 h at 70°C by adding pyridine and *N,O*-bis(trimethylsilyl)trifluoroacetamide (BSTFA) (1:1; *v/v*). The ketones and carboxylic acids did not contain any indigenous compounds and are not discussed further. Alcohol and hydrocarbon fractions were dried and re-dissolved in *n*-hexane for analyses. Compounds were identified using a Thermo Scientific Trace gas chromatograph (GC) Ultra coupled to a Thermo Scientific DSQ II mass spectrometer (MS) through comparison of retention times and published mass spectra. Quantification was achieved with a Fisons Instruments GC 8000 series equipped with a flame-ionization detector (FID). Internal standards used for quantification were 5 $\alpha$ -cholestane for the hydrocarbon fraction and 1-nonadecanol and DAGE C<sub>18-18</sub> for the alcohol fraction. The carrier gases were helium and hydrogen for the GC-MS and GC-FID analyses, respectively. Both devices were equipped with an Agilent HP-5MS UI fused silica column with a length of 30 m, a diameter of 0.25 mm and a film thickness of 0.25  $\mu$ m. The GC temperature programme was: 50°C (3 min); from 50°C to 230°C (held 2 min) at 25°C/min; then from 230°C to 320°C (held 20 min) at 6°C/min.

An aliquot of the hydrocarbon fraction was used to isolate branched and cyclic compounds from the *n*-alkanes. The aliquot was treated with 300 mg of 5 Å molecular sieve and 2 mL cyclohexane, was shaken well, then extracted by ultrasonication for 2 h. The extract was filtered and the mole sieve was repeatedly washed with cyclohexane and filtered once again to release all branched and cyclic compounds. After drying with molecular nitrogen, the extract was re-dissolved in *n*-hexane for compound identification and quantification. The GC temperature program was: 50°C (3 min); from 50°C to 230°C (held 2 min) at 25°C/min; then from 230°C to 325°C (held 25 min) at 6°C/min.

#### 3.d.1. Desulphurization with nickel boride

Desulphurization was performed for the dichloromethane-soluble fractions (asphaltenes), applying a procedure slightly modified from Schouten *et al.* (1993) and Blumenberg *et al.* (2010). Briefly, the asphaltenes were dissolved in 8 mL tetrahydrofuran/methanol (1:1, *v/v*), then 200 mg of each anhydrous nickel chloride and sodium borohydride were added. After 1 h reaction time, the samples were centrifuged and the supernatant was collected. The solid residue was extracted twice with dichloromethane/methanol (1:1, *v/v*), then centrifuged again and the supernatant was combined with the previous extract. An aqueous solution was added and the organic layer collected and dried with a rotary evaporator. The residual organic phase was filtered through dry sodium sulphate to completely remove water. Column chromatography was performed using a silica gel column and 2.5 mL of *n*-hexane/dichloromethane (9:1, *v/v*) as eluent to separate the released hydrocarbons after desulphurization from the polar compounds. The desulphurized hydrocarbon fraction was re-dissolved in *n*-hexane and the compounds identified through GC-MS analyses using the following program: from 60°C (1 min) to 150°C at 15°C/min and then up to 320°C (held 40 min) at 4°C/min. Due to low contents, the desulphurized hydrocarbon fractions were also run in single ion mode (SIM) with the masses *m/z* 133 and 546, specific masses of di-aromatic carotenoids and isorenieratane, respectively.

#### 3.d.2. Glycerol dibiphytanyl glycerol tetraether analyses

Glycerol dibiphytanyl glycerol tetraethers (GDGTs) were obtained from 10% vol. of the total lipid extract (TLE) according to the method of Hopmans *et al.* (2000) and modified by Baumann *et al.* (2018). The aliquot was dissolved in *n*-hexane and an internal standard (C<sub>46</sub> GDGT; 12 mg/L) was added. The analyses were performed using a Varian MS Workstation 6.91 high-performance liquid chromatography (HPLC) system coupled to a Varian 1200 L triple quadrupole mass spectrometer. The compounds were separated on a Grace Prevail Cyano column (150  $\times$  2.1 mm; 3  $\mu$ m particle size) and a guard column, held at 30°C. The following gradient was applied: linear change from 97.5% A (100% *n*-hexane) and 2.5% B (90% *n*-hexane; 10% 2-propanol; *v/v*) to 75% A and 25% B from 0 to 35 min; then linearly to 100% B in 5 min and held for 8 min; and thereafter, back to 97.5% A and 2.5% B to re-equilibrate the column for 12 min. The total run time was 60 min and the solvent flow was kept constant at 0.3 mL/min during the entire run time. The identification of GDGTs was achieved using a mass spectrometer equipped with an atmospheric pressure chemical ionization (APCI) interface operated in positive ion mode. The APCI parameters were: molecular nitrogen as nebulizing gas with a pressure of 60 psi; temperature fluctuating between 35°C and 40°C; 50°C as API housing temperature; 200°C for the drying gas of the API with a pressure of 12 psi; and 400°C and 18 psi for the APCI auxiliary gas temperature and pressure, respectively. The injection volume was 10  $\mu$ L. The scanned spectral range was set at *m/z* 500 to 750 and 950 to 1500. The response factors were evaluated after every 4 to 5 samples using a standard mixture containing synthetic archaeol (1,2-Di-*O*-phytanyl-*sn*-glycerol; CAS 99341-19-2), DAGE C<sub>18-18</sub> (CAS 6076-38-6), DAGE C<sub>18-18-4ene</sub> (1,3-Dilinoleoyl-*rac*-glycerol; CAS 15818-46-9) and synthetic C<sub>46</sub> GDGT (CAS 138456-87-8). The response factors between synthetic archaeol and C<sub>46</sub> GDGT were usually around 1.5:1. Relative lipid abundances were determined by selecting individual base peaks with the target mass *m/z*, including ions symmetrically with  $\pm 1.0$  of target *m/z*.

## 4. Results

### 4.a. Petrography and mineralogy

The studied interval is characterized by 8 lithological cycles of shales and argillaceous marls (referred to as marls) up to 1 m thick (Fig. 3a, b). The inorganic carbon contents range from 0.4% to 6.0%, with higher contents in marls (Fig. 3a). XRD analyses indicate that the inorganic carbon in the Govone section is composed of calcite and dolomite (see online Supplementary Material, available at <http://journals.cambridge.org/geo>). Dolomite coexists with calcite in cycles Gm26 and Gm27, while it represents the only carbonate phase in cycle Gm28 (except for sample Gm28.1) and above (Fig. 3a).

#### 4.a.1. Shales

Shales are laminated, dark-green-coloured (Fig. 3c) and rich in organic matter (TOC > 2%). They are characterized by an alternation of discontinuous, sub-millimetric, cream-coloured (type A) and dark-grey-coloured (type B) laminae, irregularly interrupted by layers up to 1.5 cm thick composed of terrigenous silt- to sand-sized grains (Fig. 4a). These layers are considered to represent the products of more intense fluvial discharge to the basin (Dela Pierre *et al.* 2014).

Type A laminae show a distinct bulbous to pinch-and-swell-type character (Fig. 4a; *sensu* Pilskaln & Pike, 2001). They are formed of two varieties of fluorescent peloids: (1) flattened to lens-shaped peloids up to 0.5 mm across with well-defined boundaries; and (2) irregular aggregates, up to 1 mm across, with irregular, diffused boundaries (Fig. 4a–c). In cycles Gm26 and Gm27, the peloids are composed of scattered silt-sized siliciclastic grains (quartz, mica flakes and feldspars), black organic matter particles and coccoliths, very abundant in the lens-shaped peloids (Fig. 4d). In cycles Gm28 to Gm33, peloids are barren of coccoliths and mostly formed of dolomite microcrystals up to 10  $\mu\text{m}$  across, scattered pyrite framboids and accessory silt-sized siliciclastic grains (Fig. 4e). Dolomite microcrystals show prevalently globular, hemispherical or cauliflower-like (*sensu* Warthmann *et al.* 2000) habits (Fig. 4e–g), and sometimes exhibit a central hollow (Fig. 4g).

Type B laminae are only a few microns thick, laterally discontinuous (Fig. 4a) and composed of silt- to clay-sized terrigenous grains (mainly quartz, feldspars and mica flakes), black amorphous organic matter debris enriched in sulphur (as revealed by EDS analyses) and abundant pyrite framboids, up to 10  $\mu\text{m}$  across. These laminae are interpreted to represent the product of enhanced terrigenous input into the basin, under the control of short-term, probably seasonal, climate change (Dela Pierre *et al.* 2014).

Both types of laminae contain scattered planktonic foraminifer tests (only in cycles Gm26 and Gm27; Fig. 4h, i), fish scales and vertebrae. Tiny (<10  $\mu\text{m}$ ) pyrite framboids (Fig. 4f–h), locally filling foraminifer tests (Fig. 4i), are abundant.

#### 4.a.2. Marls

Marls are grey-coloured (Fig. 3d) with bioturbation only present in the pre-MSC cycles (Fig. 5a). Marls are rich in silt-sized terrigenous grains (mainly quartz, feldspar and mica flakes), and contain finely dispersed pyrite grains up to 10  $\mu\text{m}$  across (framboids and octahedral crystals; Fig. 5b, c). Dolomite is common in the MSC cycles, consisting of globular and cauliflower-like (Fig. 5d–f) microcrystals, up to 20  $\mu\text{m}$  across, often typified by a central hollow (Fig. 5e, f). Dumbbell-shaped crystals also occur (Fig. 5f).

### 4.b. Carbon and oxygen stable isotopes

The bulk-rock  $\delta^{13}\text{C}$  values range from  $-5.2\text{‰}$  to  $+0.3\text{‰}$ , lacking an obvious relationship with lithology (Fig. 3; online Supplementary Material, available at <http://journals.cambridge.org/geo>). However, a general trend towards more negative  $\delta^{13}\text{C}$  values is observed across the MSC onset, evidenced by overall more pronounced  $^{13}\text{C}$ -depletion in MSC cycles (average  $\delta^{13}\text{C} = -2.4\text{‰}$ ) than in pre-MSC cycles (average  $\delta^{13}\text{C} = -1.0\text{‰}$ ). A moderate negative correlation was found when plotting the bulk-rock  $\delta^{13}\text{C}$  values of shales ( $n = 6$ ) and marls ( $n = 7$ ) against the TIC contents, where dolomite was the only carbonate phase detected (shales,  $r = -0.7$ ; marls,  $r = -0.6$ ; online Supplementary Material). The  $\delta^{18}\text{O}$  bulk-rock values vary from  $-4.5\text{‰}$  to  $+5.5\text{‰}$ . As for  $\delta^{13}\text{C}$  values, a correlation with lithology was not observed (Fig. 3). The largest fluctuations were found in the pre-MSC cycles ( $+5.4\text{‰} \geq \delta^{18}\text{O} \geq -4.5\text{‰}$ ), while the MSC cycles show less variable, positive  $\delta^{18}\text{O}$  values (average  $+3.5\text{‰}$ ; Fig. 3).

### 4.c. Total organic carbon contents and lipid biomarkers

The TOC contents vary from 1.0% to 3.1% (Fig. 6; online Supplementary Material, available at <http://journals.cambridge.org/geo>) and follow lithological cyclicity, with higher contents in shales (average 2.4%) and lower contents in marls (average 1.6%), particularly in pre-MSC cycles (as low as 1.0%).

#### 4.c.1. Archaeol and GDGT distribution and caldarchaeol/crenarchaeol ratio

GDGTs and  $\text{C}_{20-20}$  archaeol (archaeol) were detected in the Govone samples. The former are mainly represented by GDGT-0 (caldarchaeol) and GDGT-5 (crenarchaeol), with relative contents ranging from 18.0% to 31.2% and 18.3% to 32.9% of the total GDGTs plus archaeol assemblage, respectively (Fig. 6, Table 1; online Supplementary Material, available at <http://journals.cambridge.org/geo>). GDGTs with 1–3 cyclopentane rings and GDGT-5' (crenarchaeol isomer) yielded relative contents of  $\leq 11.0\%$  on average (Fig. 6, Table 1). Archaeol revealed relative contents between 7.8% and 42.9% of the total GDGTs plus archaeol inventory (Fig. 6, Table 1, online Supplementary Material). The distribution of GDGTs and archaeol did not vary across the MSC onset (Fig. 6, Table 1). The caldarchaeol/crenarchaeol ratio varies between 0.8 and 1.5, with an average of 1.1 (Fig. 6; online Supplementary Material).

#### 4.c.2. Acyclic and cyclic triterpenoids and the lycopane/ $n\text{-C}_{31}$ alkane ratio

The hydrocarbon and alcohol fractions contain, among other compounds ( $n$ -alkanes and  $n$ -alkanols, steranes and sterols, hopanes and hopanols, long-chain diols and keto-ols; thiolanes, thianes and thiophenes; data not shown), the acyclic triterpenoid lycopane and the pentacyclic triterpenoid tetrahymanol.

Lycopane, isolated with a molecular sieve from the  $n$ -alkanes, was found in most of the 18 samples (except for marls in cycle Gm26), yielding varying contents (up to 25.0  $\mu\text{g/g}$  TOC). In general, shales revealed much higher contents than marls (Fig. 6, Table 1; online Supplementary Material, available at <http://journals.cambridge.org/geo>). Lycopane contents increase upwards, especially above the MSC onset (Fig. 6). The lycopane/ $n\text{-C}_{31}$  alkane ratio, a palaeo-oxicity proxy introduced by Sinninghe Damsté *et al.* (2003), ranges from 0.01 to 1.2 (online Supplementary Material) with most ratios < 0.3; such values suggest that the seafloor was constantly oxygenated (*cf.* Sinninghe



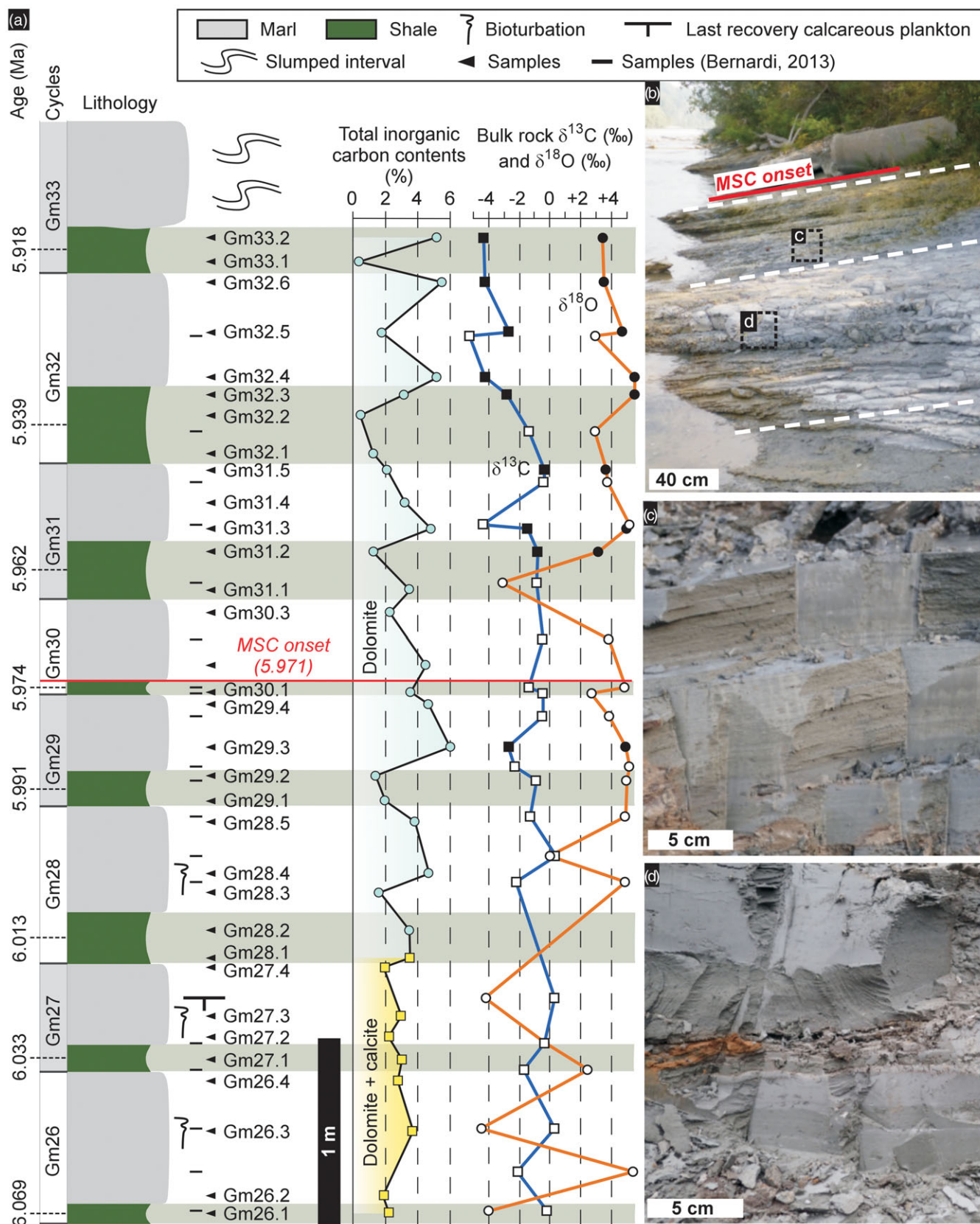


**Fig. 3.** (Colour online) (a) The Govone section with sample locations, total inorganic carbon contents, carbonate mineralogy and bulk-rock carbon ( $\delta^{13}\text{C}$ ) and oxygen ( $\delta^{18}\text{O}$ ) stable isotope values. White squares and circles refer to  $\delta^{13}\text{C}$  and  $\delta^{18}\text{O}$  values from Bernardi (2013), whereas black squares and circles refer to values from this study. (b) Outcrop view of the Govone section. The red line corresponds to the onset of the MSC; the white dashed lines indicate the top of marl beds; insets indicate the position of figures (c) and (d). (c) Close-up of pre-MSC laminated organic-rich shales. (d) Close-up of pre-MSC homogenous marls.



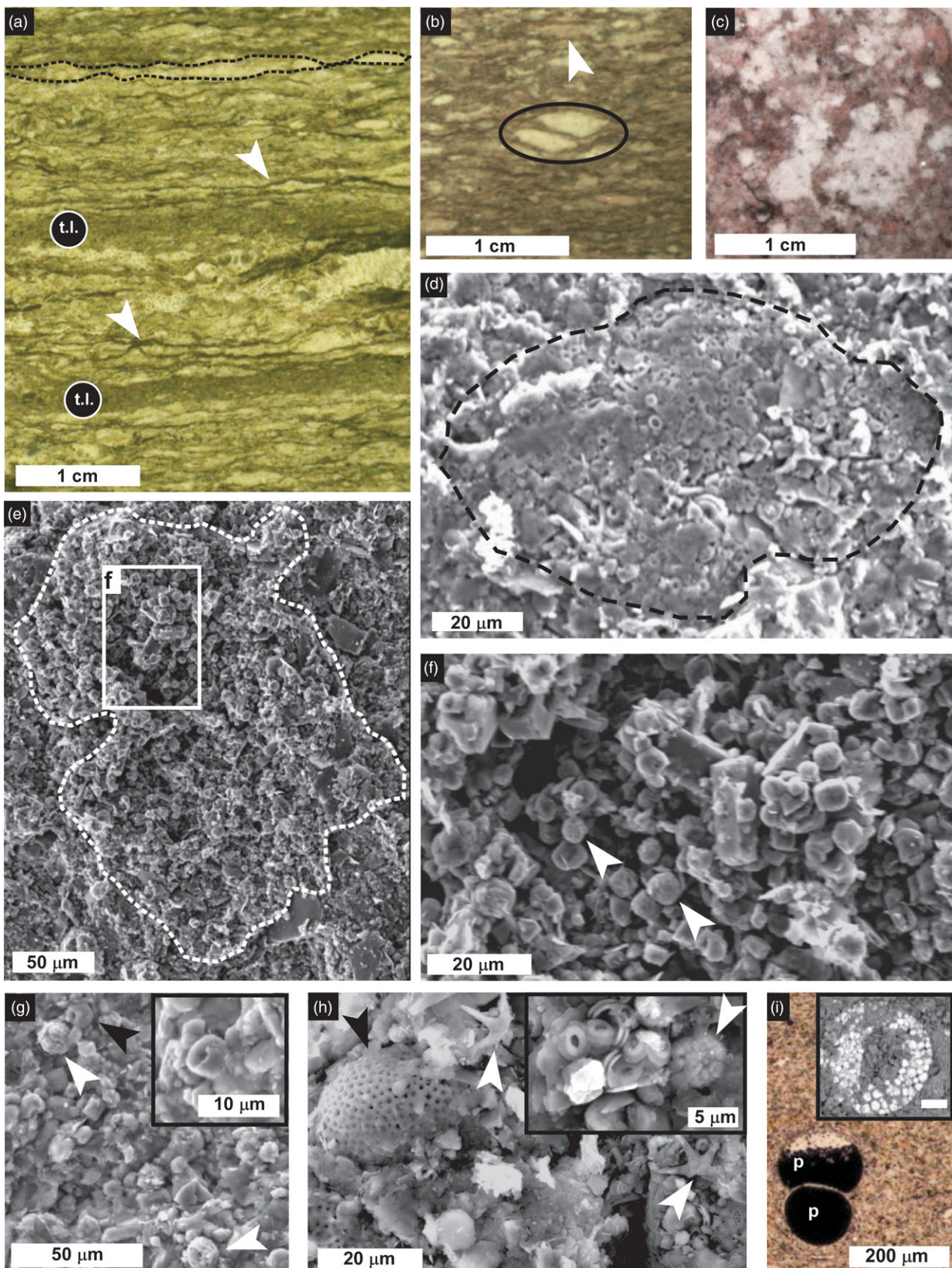


**Fig. 4.** (Colour online) Organic-rich shales. (a) Polished slab cut perpendicular to bedding. Type A and B laminae separated by coarser terrigenous layers (t.l.). The black dashed lines envelope a type A lamina, the white arrows indicate two type B laminae. (b) Fluorescent, lens-shaped faecal pellets (black oval) and flattened, faintly fluorescent aggregate (white arrow); UV-fluorescence image. (c) Irregular aggregates cut parallel to bedding; UV-fluorescence image. (d) Faecal pellet (dashed line) composed of coccoliths; SEM micrograph. (e) Irregular aggregate (dashed line) mostly composed of dolomite microcrystals from the MSC part of the section. The white box indicates the position of (f); SEM micrograph. (f) Globular dolomite microcrystals and scattered pyrite framboids (white arrows); SEM micrograph. (g) Hollow dolomite microcrystals (black arrow and inset) and scattered pyrite framboids (white arrows); SEM micrograph. (h) Planktonic foraminifer test (black arrow) surrounded by coccoliths (white arrows). The inset shows a detail with coccoliths and a small pyrite framboid (arrow); SEM micrograph. (i) Foraminifer test partially filled with pyrite (p); plane-polarized light. The inset is a backscattered electron image of a pyrite infilling, consisting of an aggregate of tiny pyrite framboids. Scale bar in the inset is 20  $\mu\text{m}$ .



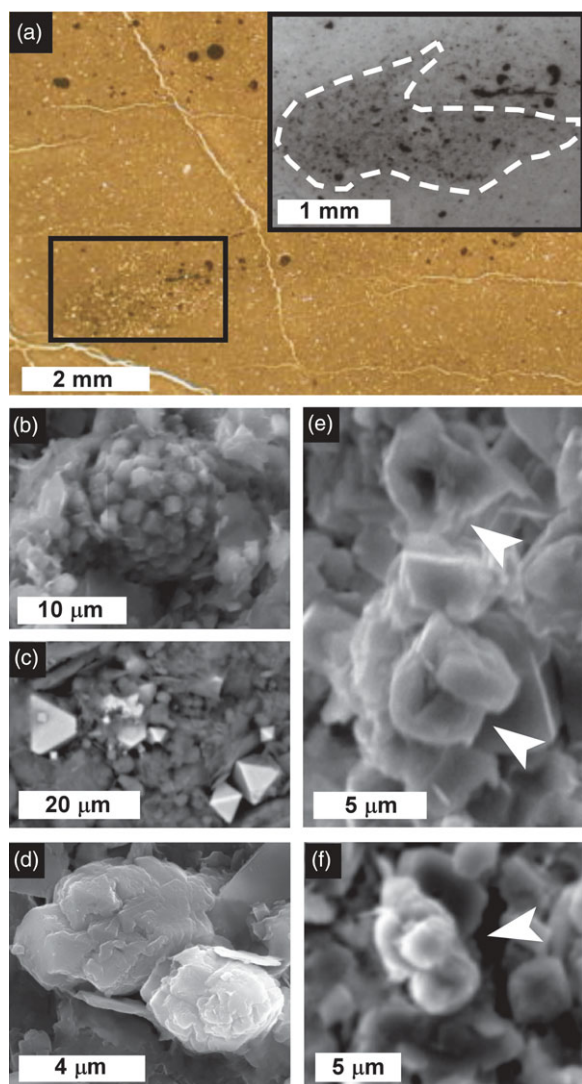


**Fig. 5.** (Colour online) (a) Photomicrographs and (b–f) SEM images of marls. (a) Bioturbation traces in pre-MSC marl (black box); the inset is a close-up image in UV light of the bioturbation traces, highlighted by dashed line. Pyrite: (b) framboid, (c) octahedral crystals. Dolomite microcrystals with (d) cauliflower, (e) globular and (f, arrow) dumbbell-like shapes. The arrows in (e) indicate central hollows in dolomite microcrystals.

Damsté *et al.* 2003), although petrographic and other organic geochemical evidence suggests the opposite (see Section 5.c below). This inconsistency most likely results from the high flux of leaf-wax-derived long-chain *n*-alkanes relative to lycopane, which can significantly affect the ratio and make the use of its absolute values unreliable (*cf.* Sinninghe Damsté *et al.* 2003). We therefore decided not to apply the absolute values of the ratio, as suggested by Sinninghe Damsté *et al.* (2003), but refer to trends between the lithologies to infer relative variations in palaeo-oxicity.

Tetrahymanol occurs in all samples with contents ranging from 1.1 to 26.5  $\mu\text{g/g}$  TOC (Fig. 6; online Supplementary Material, available at <http://journals.cambridge.org/geo>). Tetrahymanol is more abundant in shales than in marls, although the difference between the two lithologies is less pronounced in the MSC interval than in the pre-MSC part of the section (Fig. 6, Table 1; online Supplementary Material).

#### 4.c.3. Hydrocarbons liberated after desulphurization

The desulphurization of asphaltenes released mostly *n*-alkanes ( $C_{14}$  to  $C_{40}$ ), a pentacyclic  $C_{30}$  sulphide (*cf.* Poinsoot *et al.* 1998) and, especially in shales, phytane. As well as these compounds, we identified  $C_{27}$  to  $C_{29}$  steranes,  $C_{31}$  to  $C_{35}$  hopanes, and, only in samples from cycles Gm28 to Gm30, the diaromatic carotenoid isorenieratane. In most cases (with the exception of sample Gm30), isorenieratane was identified in single ion mode (SIM) only ( $m/z$  133 and 546). This is in accordance with very low contents, rendering quantification impossible.

## 5. Discussion

### 5.a. Water-column stratification and euxinia across the onset of the MSC

The restriction of the Mediterranean leading to the MSC was associated with an intensification of water-column stratification (Roveri *et al.* 2014) that persisted during the entire MSC event (Christeleit *et al.* 2015; Simon & Meijer, 2017; García-Veigas *et al.* 2018). The same evolution has been reconstructed for the Piedmont Basin (Dela Pierre *et al.* 2011; Bernardi, 2013; Violanti *et al.* 2013; Lozar *et al.* 2018), especially by the study of the Pollenzo section, a section about 20 km SW from the Govone section (Natalicchio *et al.* 2017, 2019). For the Pollenzo section, the most compelling evidence of increasing water-column stratification after the MSC onset is the appearance of tetrahymanol. This compound is produced by organisms commonly thriving at chemoclines (Wakeham *et al.* 2012), namely bacterivorous ciliates, anoxygenic phototrophic bacteria and aerobic methanotrophic bacteria (Kleemann *et al.* 1990; Harvey & McManus, 1991; Rashby *et al.* 2007; Eickhoff *et al.* 2013; Banta *et al.* 2015; Cordova-Gonzales *et al.* 2020); tetrahymanol is therefore considered a robust indicator of water-column stratification (*e.g.* Sinninghe Damsté *et al.* 1995b).

Tetrahymanol was found throughout the section at Govone, suggesting that, in the more distal settings of the Piedmont Basin, stratified conditions had already been established before the onset of the MSC. The higher tetrahymanol contents in shales suggest that stratification was more intense at precession minima, most likely in response of enhanced riverine runoff (*cf.* Natalicchio *et al.* 2019; Sabino *et al.* 2020). Enhanced riverine runoff in turn promoted episodes of high productivity and phytoplankton blooms. The latter are testified by the very abundant lens-shaped peloids and irregular aggregates, which have been interpreted as faecal pellets and marine snow-flakes, respectively (*cf.* Dela Pierre *et al.* 2014), both main components of so-called marine snow (*e.g.* Alldredge & Silver, 1988; Alldredge *et al.* 2002). Interestingly, in the shales of the uppermost pre-MSC cycles (Gm28–30), tetrahymanol is accompanied by isorenieratane, derived from the degradation of isorenieratene sourced by green sulphur bacteria (Repeta *et al.* 1989; Van Gernerden & Mas, 1995). These phototrophic bacteria require hydrogen sulphide to perform anoxygenic photosynthesis (*e.g.* Van Gernerden & Mas, 1995) and are found in modern stratified basins when sulphidic conditions extend into the photic zone (*e.g.* Black Sea, Sinninghe Damsté *et al.* 1993; Wakeham *et al.* 2007; Cariaco Basin, Wakeham *et al.* 2012), making isorenieratene and its derivatives biomarkers for photic zone euxinia (*e.g.* Repeta & Simpson, 1991; Kuypers *et al.* 2002). The co-occurrence of tetrahymanol and isorenieratane in shales therefore supports pronounced water-column stratification at

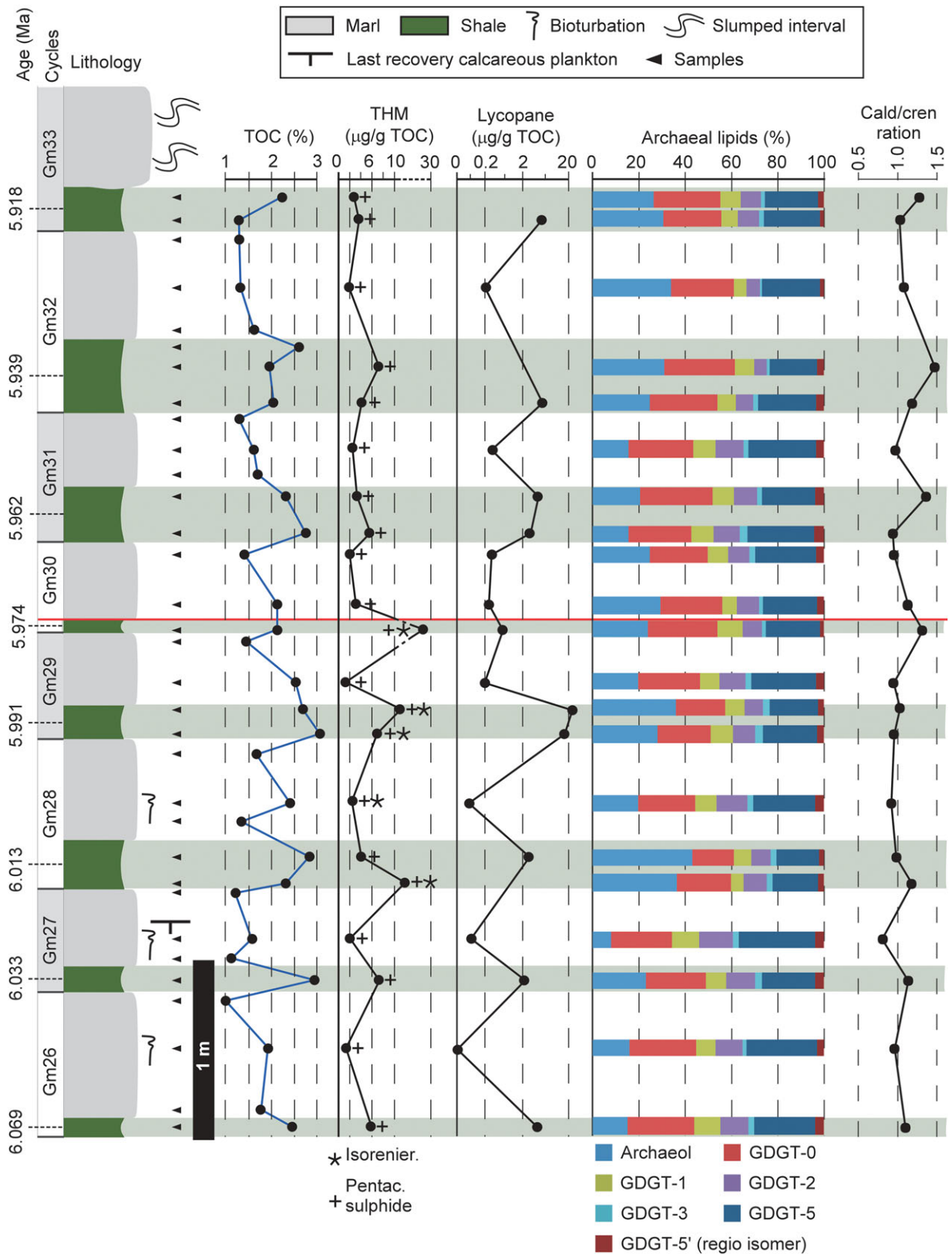


**Fig. 6.** (Colour online) TOC contents, lipid biomarker distributions and caldarchaeol/crenarchaeol ratio (cald/cren ratio) across the onset of the Messinian salinity crisis in the Govone section. Note pentacyclic C<sub>30</sub> sulphide (Pentac. sulphide) and isorenieratane (isorenier.) in the tetrahymanol distribution profile and the non-metric scale in the lycopane distribution profile. The red line at the base of marls in cycle Gm30 indicates the onset of the Messinian salinity crisis. GDGT - glycerol dibiphytanyl glycerol tetraethers; Ly - lycopane; THM - tetrahymanol; GDGT-0 - caldarchaeol; GDGT-5 - crenarchaeol.



**Table 1.** Archaeol, GDGTs (both in % relative to all GDGTs plus archaeol), lycopane and tetrahymanol abundances in pre-MSC and MSC Govone sediments. Max = maximum content, Min = minimum content, GDGT-0 = caldarchaeol, GDGT-5 = crenarchaeol.

	Max (%)	Min (%)	Average pre-MSC (%)	Average MSC (%)
GDGT-0	31.2	18.0	25.2	27.9
GDGT-1	11.9	5.4	9.0	8.2
GDGT-2	14.5	5.6	11.0	8.9
GDGT-3	3.1	1.0	2.5	1.9
GDGT-5	32.9	18.3	24.8	24.8
GDGT-5' (regio isomer)	4.2	1.8	3.2	3.1
C <sub>20-20</sub> archaeol	42.9	7.8	24.4	25.1
	Max (µg/g TOC)	Min (µg/g TOC)	Average Pre-MSC (µg/g TOC)	Average MSC (µg/g TOC)
Lycopane	25.0	0.1	9.7	6.6
Shales			0.1	0.3
Marls				
Tetrahymanol	26.5	1.1	10.6	4.6
Shales			1.7	2.3
Marls				

precession minima already before the onset of the MSC, occasionally accompanied by photic zone euxinia. The lower contents of tetrahymanol and the lack of isorenieratane in the MSC shales apparently suggest the weakening of stratification, which is however in contrast with evidence from the neighbouring Pollenzo section (Natalicchio *et al.* 2017, 2019). This inconsistency could reflect unfavourable environmental conditions at precession minima for the producers of isorenieratane and tetrahymanol after the MSC onset in the distal part of the basin (Govone), rather than the weakening of water-column stratification. Interestingly, in modern stratified basins, ciliates are found to feed, among other organisms, on green sulphur bacteria (Wakeham *et al.* 2007, 2012). The trophic relationship between autotrophic green sulphur bacteria and heterotrophic ciliates, already inferred for the MSC sediments of the Northern Apennines (Vena del Gesso Basin, Sinninghe Damsté *et al.* 1995a), can potentially explain the trend of compound contents in the Govone section, where tetrahymanol peaks coincide with the presence of isorenieratane. Adverse conditions for green sulphur bacteria were most likely related to an intensified input of terrigenous material by rivers after the MSC onset, as evidenced by increasing contents of terrestrial plant waxes (Natalicchio *et al.* 2019; Sabino *et al.* 2020). Enhanced riverine runoff might have increased turbidity and input of oxygen in the upper water column, both deleterious factors for phototrophic green sulphur bacteria (Van Gemerden & Mas, 1995), in turn causing a decrease of the ciliate population.

Evidence of persistent stratification and sulphidic conditions in the water column at precession minima after the MSC onset, although not extending into the photic zone, is provided by the occurrence of small pyrite framboids and sulphur-enriched organic matter. The small size of the super-abundant pyrite framboids (< 10 µm) may suggest that they formed within an euxinic water column (*cf.* Wilkin *et al.* 1996; Passier *et al.* 1997; Bond & Wignall, 2010; Tagliavento *et al.* 2020). Organic sulphur compounds, such as the pentacyclic C<sub>30</sub> sulphide, are believed to form during a very early diagenetic stage, possibly already in the water column when reduced-sulphur species (e.g. hydrogen sulphide) exceed reduced iron and consequently bind to settling organic matter (Sinninghe Damsté & de Leeuw, 1990; Wakeham *et al.* 1995; Poinot *et al.* 1998).

Compared with shales, marls reveal lower contents of tetrahymanol. Such a pattern reflects the weakening of stratification at precession maxima in response to more efficient mixing of the water column (e.g. Sierro *et al.* 2001; Violanti *et al.* 2013). Mixing was promoted by drier climate conditions and reduced fluvial discharge, in accordance with higher element/Al ratios and a decrease of contents in the sediments of terrestrial plant waxes, which show deuterium enrichment (Sabino *et al.* 2020). However, water-column stratification never completely ceased to exist, since the occurrence of small pyrite framboids and sulphur organic compounds suggests that sulphidic conditions were intermittently present in the water column. The trend to slightly higher tetrahymanol contents in MSC marls compared with pre-MSC marls suggests that water-column stratification was more intense at precession maxima after the onset of the MSC compared with precession maxima during the pre-MSC, in agreement with the appearance of tetrahymanol in time-equivalent more marginal sediments (Pollenzo section; Natalicchio *et al.* 2017). This was possibly due to the establishment of a wetter climate in the northern Mediterranean (*cf.* Natalicchio *et al.* 2019; Sabino *et al.* 2020).

### 5.b. Persistence of marine conditions in surface waters after the onset of the MSC

The Govone section is characterized by the progressive decline and final disappearance of calcareous plankton approaching the MSC onset (Bernardi, 2013). Such ecological change is recorded in other sections across the Mediterranean and was taken as evidence of progressively harsher conditions in surface waters, with fluctuations of salinity up to high levels not tolerated by most marine biota (e.g. Sierro *et al.* 1999; Blanc-Valleron *et al.* 2002; Manzi *et al.* 2007). The establishment of hypersaline conditions during the MSC is also reflected by the archaeal di- and tetraether lipid assemblages of MSC carbonates from Sicily and Calabria (the so-called 'Calcare di Base'); in these deposits, C<sub>20-20</sub> archaeol, C<sub>20-25</sub> archaeol (extended archaeol) and caldarchaeol dominate the isoprenoid diphytanyl glycerol diether (DGD) and GDGT inventories (Turich & Freeman, 2011; Birgel *et al.* 2014).

In contrast, the isoprenoid DGD and GDGT distribution found for the Govone section is significantly different from that of the

Calcare di Base and does not agree with widespread hypersalinity after the onset of the MSC. In fact, archaeol does not dominate over the total GDGTs (*c.* 25% of the total GDGT and DGD lipid inventory) and is never accompanied by extended archaeol, allowing the exclusion of a significant contribution from halophilic archaea (*cf.* Teixidor *et al.* 1993; Dawson *et al.* 2012). Possible alternative sources for archaeol are non-halophilic archaea, such as methanogens, methanotrophs and marine Euryarchaeota thriving in epi- to mesopelagic zones (De Rosa & Gambacorta, 1988; Blumenberg *et al.* 2004; Turich *et al.* 2007; Sollai *et al.* 2019). Methanogenic and methanotrophic archaea, on the other hand, can be excluded for the Govone section, since the distribution of isoprenoidal di- and tetraether lipids varies from those observed in methane-seep environments, the latter typified by the dominance of archaeol, hydroxyarchaeol and GDGT-1 and 2 over the other dibiphytanyl tetraethers (De Rosa & Gambacorta, 1988; Blumenberg *et al.* 2004; Wakeham *et al.* 2007). Consequently, marine Euryarchaeota thriving in the epi- to mesopelagic zones of a normal marine water column are the most likely source of archaeol (*cf.* Turich *et al.* 2007; Schouten *et al.* 2008; Elling *et al.* 2015; Sollai *et al.* 2019). Interestingly, it has been suggested that mesopelagic marine Euryarchaeota from the group III (MGIII) are important producers of archaeol, especially in oxygen-deficient zones where they can even dominate the archaeal community (Belmar *et al.* 2011; Sollai *et al.* 2019). Since episodic oxygen deficiency seems to have characterized the water column of the Piedmont Basin during the MSC, mesopelagic marine Euryarchaeota are the most likely source of archaeol in the Govone section, indicating the persistence of marine rather than hypersaline conditions across the onset of the MSC.

Marine conditions are in accordance with the distribution of the GDGTs and the caldarchaeol/crenarchaeol ratio (*c.* 1), which mirror the distribution and the ratios reported for open-ocean settings (e.g. Turich *et al.* 2007; Kim *et al.* 2010; Pearson & Ingalls, 2013; Schouten *et al.* 2013). Under such conditions, the main contributors to the GDGT pool are planktonic marine Euryarchaeota of the group II (MGII) and Thaumarchaeota (marine group I, MGI), dwelling in the epi- to mesopelagic zones (Schouten *et al.* 2013; Santoro *et al.* 2019). Despite some controversy (Lincoln *et al.* 2014; Schouten *et al.* 2014), MGII archaea are thought to source mostly acyclic GDGTs (caldarchaeol), whereas MGI archaea synthesize both acyclic and polycyclic GDGTs, especially crenarchaeol (Elling *et al.* 2017; Zeng *et al.* 2019). This pattern results in the dominance of caldarchaeol and crenarchaeol over the other GDGTs and a caldarchaeol/crenarchaeol ratio of *c.* 1 (Sinninghe Damsté *et al.* 2002; Schouten *et al.* 2013 for a review), which closely mirror the tetraether archaeal lipid distribution and the ratio of marine planktonic Thaumarchaeota growing in cultures at normal salinity (*c.* 35‰ salinity; Elling *et al.* 2015).

The persistence of marine conditions in surface waters challenges the idea of an establishment of a completely hypersaline water mass early on during the MSC (e.g. Bellanca *et al.* 2001). The lack of pervasive hypersaline conditions agrees with (1) the presence of marine fossils (foraminifers, calcareous nannoplankton, diatoms, fishes) above the MSC onset in more marginal sections of the Piedmont Basin (Violanti *et al.* 2013; Dela Pierre *et al.* 2014; Lozar *et al.* 2018; Carnevale *et al.* 2019) and (2) palaeosalinity estimates from gypsum fluid inclusions, indicating that the parent brine had a salinity possibly even lower than seawater (Natalicchio *et al.* 2014). In this light, the disappearance of calcareous plankton in the Govone section two cycles below the onset of the MSC most likely reflects diagenetic dissolution of calcareous skeletons rather

than harsh environmental conditions in superficial waters (Dela Pierre *et al.* 2014).

### 5.c. Fluctuations in oxygen concentration of bottom waters across the onset of the MSC

Intensification of water-column stratification in the Mediterranean Basin shortly before the onset of the MSC was associated with widespread depletion of oxygen in bottom waters, which is recorded by the precession-driven deposition of organic-rich sediments (Hilgen & Krijgsman, 1999; Krijgsman *et al.* 2001, 2002) and by the replacement of oxyphilic benthic foraminifera with stress-tolerant taxa (e.g. Kouwenhoven *et al.* 1999; Blanc-Valleron *et al.* 2002; Gennari *et al.* 2018). Such a trend was confirmed for the Piedmont Basin by changes in the assemblages of benthic foraminifers in the pre-MSD sediments (Bernardi, 2013; Violanti *et al.* 2013). However, very little information is available for the microfossil-poor or microfossil-barren MSC strata.

The Govone section archives the fluctuation of oxygen contents at the seafloor driven by precessional forcing. Humid climate and enhanced riverine runoff at precession minima (Natalicchio *et al.* 2019; Sabino *et al.* 2020) favoured intense water-column stratification and bottom anoxia, which is witnessed by the deposition of laminated, organic-rich shales (TOC > 2%). Evidence of bottom-water anoxia during the deposition of shales includes their high contents of lycopane. Studies of modern (Wakeham *et al.* 1993; Sinninghe Damsté *et al.* 2003) and ancient sediments (e.g. Freeman *et al.* 1990; Kenig *et al.* 1995; Behrooz *et al.* 2018; Löhr *et al.* 2018) have shown that preservation of lycopane is highest when bottom waters are anoxic.

Lower TOC contents (mostly < 2%) and the sharp drop of lycopane contents ( $\leq 0.4 \mu\text{g/g}$  TOC) in marls indicate higher oxygen levels at the seafloor than at times of shale deposition, reflecting precession-driven climate change (Sabino *et al.* 2020). However, changes can be observed across the onset of the MSC, possibly recording different degrees of bottom-water ventilation before and after the advent of the crisis. In particular, pre-MSD marls show bioturbation traces and contain few stress-tolerant benthic foraminifers (Bernardi, 2013; Dela Pierre *et al.* 2016), suggesting that the seafloor was at least episodically oxygenated. In contrast, the absence of bioturbation and the slight increase of lycopane contents in MSC marls compared with pre-MSD marls indicate that bottom waters became progressively oxygen depleted, agreeing with an intensification of water-column stratification at precession maxima during the MSC relative to precession maxima in pre-MSD times (Section 5.a above). Despite such a trend to lower oxygen levels, the only low lycopane contents at precession maxima compared with precession minima (shale deposition) suggest that bottom waters were not fully anoxic during the deposition of marls (*cf.* Sinninghe Damsté *et al.* 2003).

### 5.d. Primary Lower Gypsum: implications on depositional environments and stratigraphic architecture

The integration of geochemical, sedimentological and petrographic data indicates that during the early phase of the MSC the water column in the Piedmont Basin was stratified and comprised (1) an oxygenated upper layer, typified by mostly marine conditions and receiving input of freshwater from rivers (Natalicchio *et al.* 2019; Sabino *et al.* 2020) and/or low-salinity water from the Paratethys (Grothe *et al.* 2020); and (2) an anoxic to euxinic lower layer, formed by denser, more saline waters (Dela Pierre *et al.* 2014; Natalicchio *et al.* 2017), the latter agreeing with



more positive  $\delta^{18}\text{O}$  values (average +3.5‰) of MSC sediments. The two water masses were separated by a pycnocline, at which chemical gradients established with time and a chemocline developed, as observed for modern basins (Wakeham *et al.* 2007, 2012) and reconstructed for ancient basins with stratified water masses (e.g. the Badenian basin of Eastern Europe; Babel, 2004; Babel & Bogucki, 2007).

Stratigraphic data reveal a lateral facies change in the PLG unit from the margin to the depocentre of the Piedmont Basin for sediments deposited during precession maxima (Dela Pierre *et al.* 2011). Bottom-grown selenite gypsum is observed only in the shallow, marginal part of the basin (Arnulfi section; Fig. 7). Moving towards the depocentre, gypsum makes lateral transition to marls and carbonates with filamentous fossils (Pollenzo section; Fig. 7) – interpreted to represent chemotrophic microbial mats (Dela Pierre *et al.* 2012) – and finally to dolomite-rich marls (Govone section; Fig. 7). Conversely, at precession minima, organic-rich shales were deposited across the entire Piedmont Basin (Dela Pierre *et al.* 2011, 2016; Fig. 7). We suggest that these stratigraphic patterns reflect vertical chemocline oscillations controlled by precession (Fig. 7).

The widespread seafloor anoxia recorded by shales indicates that the chemocline was located above the sea bottom across most of the basin during precession minima. These conditions favoured organic matter preservation in the water column and led to an increased sedimentation of organic matter, which, in turn, favoured heterotrophic, bacterial sulphate reduction and promoted bacterially mediated precipitation of early diagenetic dolomite in anoxic, organic-rich sediments (Fig. 7a). This inference agrees with (1) the negative bulk-rock  $\delta^{13}\text{C}$  values (*cf.* Petrash *et al.* 2017); (2) the moderate negative correlation ( $r = -0.7$ ) between TIC contents, represented by dolomite, and bulk-rock  $\delta^{13}\text{C}$  values (high TIC contents coincide with low  $\delta^{13}\text{C}$  values); and (3) dolomite crystal habits (Figs 4f, g, 5d–f; *cf.* Warthmann *et al.* 2000; van Lith *et al.* 2003; Sanz-Montero *et al.* 2008; Bontognali *et al.* 2010; Han *et al.* 2016).

The change towards a less humid climate at precession maxima (Sabino *et al.* 2020) resulted in the deepening of the chemocline and the thinning of the anoxic zone (Fig. 7b). Under these circumstances, selenite grew only in the shallower part of the basin (Arnulfi section, Fig. 7b), where low-salinity waters enriched in calcium and sulphate ions, possibly derived from leaching of former evaporites (Natalicchio *et al.* 2014), occurred above an oxygenated sea bottom (e.g. García-Veigas *et al.* 2018). In more distal settings, the absence of gypsum was possibly related to low-oxygen conditions, which favoured bacterial sulphate reduction and resultant gypsum undersaturation (Fig. 7b; *cf.* Babel, 2004; de Lange & Krijgsman, 2010; García-Veigas *et al.* 2018). The parts of the basin where the chemocline impinged on the seafloor (Pollenzo section, Fig. 7b; Natalicchio *et al.* 2017) were covered by microbial mats of putative sulphide-oxidizing bacteria (Natalicchio *et al.* 2017). In modern settings, these bacteria thrive under hypoxic conditions where the chemocline intercepts the seafloor and steep gradients between electron acceptors and hydrogen sulphide occur (e.g. the Black Sea; Jessen *et al.* 2016). In contrast, in deeper parts of the basin (Govone section; Fig. 7b) the sea bottom was in contact with more reducing waters. These conditions favoured the preservation of organic matter in the water column, enhanced the deposition of organic matter at the seafloor and led to an increase in bacterial sulphate reduction in the sediments, which triggered the widespread precipitation of early diagenetic microbial dolomite (Fig. 7b).

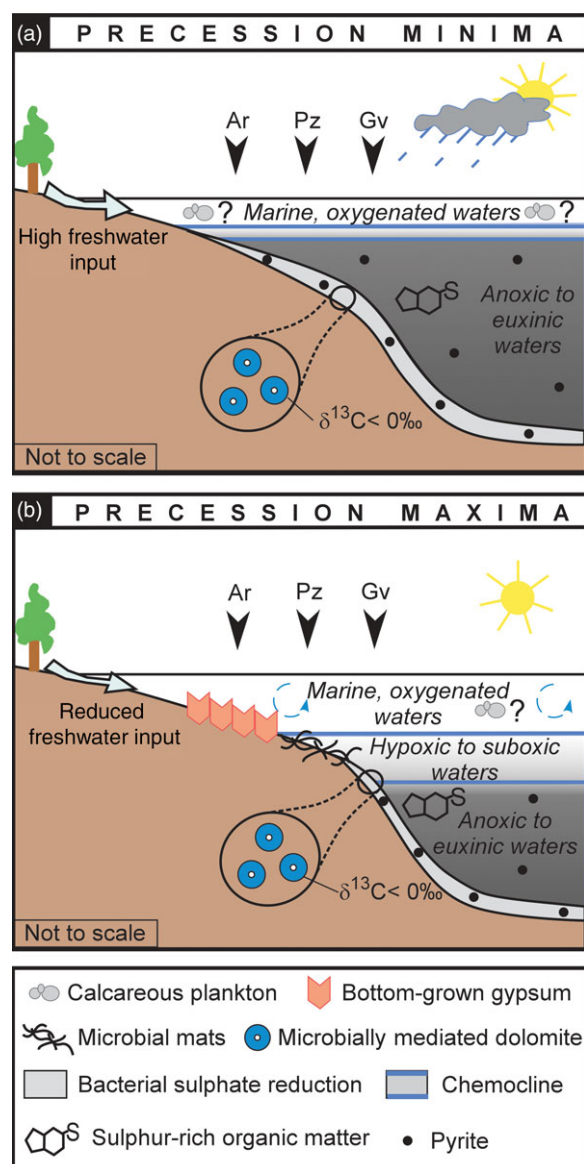


**Fig. 7.** (Colour online) Reconstruction of the water-column structure of the Piedmont Basin at (a) precession minima, insolation maxima and shale deposition and (b) precession maxima, insolation minima and marl deposition during the earliest phase of the Messinian salinity crisis. The black arrows indicate the positions of sections (Ar: Arnulfi; Pz: Pollenzo; Gv: Govone). The thickness of the chemocline is emphasized in (b) to highlight the different conditions described in the text.

## 6. Conclusions

Hydrological change affecting the Piedmont Basin during the early stages of the Messinian salinity crisis (MSC) led to an intensification of water-column stratification. The water column was divided into denser, more saline and oxygen-depleted bottom waters separated by a chemocline from an upper water layer consisting of oxic seawater influenced by freshwater inflow. No evidence of a sharp increase of salinity across the MSC onset was found. Vertical oscillations of the chemocline exerted control over the stratigraphic architecture of the Primary Lower Gypsum unit and its deeper-water equivalents deposited during the first stage of the MSC. This study documents how temporal and spatial changes of water masses with different redox chemistries must be carefully considered when interpreting the MSC event.

**Acknowledgements.** We thank S. Beckmann (Universität Hamburg) for technical support during organic geochemical analyses, L. Baumann (Universität Hamburg) for support in the application of the GDGTs proxies, D. Bortels (Universität Hamburg) for help with lipid biomarker extraction, J. Richarz (Universität Hamburg) for the analysis of TOC contents and H. Kuhnert (University of Bremen) for the bulk-rock carbon and oxygen stable isotopes analyses and help with data processing. S. Cavagna (University of Torino) is thanked for support with SEM-EDS analyses. This project received funding from University of Torino grants (ex 60% 2017 and 2019) to F. Dela Pierre. M. Sabino is funded by a doctoral scholarship provided by the Landesgraduiertenförderung of the state of Hamburg. The article is based upon work towards COST (European Cooperation in Science and Technology) Action ‘Uncovering the Mediterranean salt giant’ (MEDSALT). Comments by Iuliana Vasiliev and an anonymous reviewer helped to improve the manuscript.

**Declaration of Interest.** None.

**Supplementary material.** To view supplementary material for this article, please visit <https://doi.org/10.1017/S0016756820000874>

## References

- Allredge AL and Silver MW (1988) Characteristics, dynamics and significance of marine snow. *Progress in Oceanography* **20**, 41–82.
- Allredge AL, Cowles TJ, MacIntyre S, Rines JEB, Donaghay PL, Greenlaw CF, Holliday DV, Deksheniaks MM, Sullivan JM and Zaneveld JRV (2002) Occurrence and mechanisms of formation of a dramatic thin layer of marine snow in a shallow Pacific fjord. *Marine Ecology Progress Series* **233**, 1–12.
- Babel M (2004) Models for evaporite, selenite and gypsum microbialite deposition in ancient saline basins. *Acta Geologica Polonica* **54**, 219–49.
- Babel M and Bogucki A (2007) The Badenian evaporite basin of the northern Carpathian Foredeep as a model of a meromictic selenite basin. In *Evaporites Through Space and Time* (eds BC Schreiber, S Lugli and M Babel, pp. 219–46. Geological Society of London, Special Publication no. 285.
- Banta AB, Wei JH and Welander PV (2015) A distinct pathway for tetrahydromanol synthesis in bacteria. *Proceedings of the National Academy of Sciences* **112**, 13478–83.
- Baumann LMF, Taubner RS, Bauersachs T, Steiner M, Schleper C, Peckmann J, Rittmann SK-MR and Birgel D (2018) Intact polar lipid and core lipid inventory of the hydrothermal vent methanogens *Methanocaldococcus villosus* and *Methanothermococcus okinawensis*. *Organic Geochemistry* **126**, 33–42.
- Behrooz L, Naafs BDA, Dickson AJ, Love GD, Batenburg SJ and Pancost RD (2018) Astronomically driven variations in depositional environments in the South Atlantic during the Early Cretaceous. *Paleoceanography and Paleoclimatology* **33**, 894–912.
- Bellanca A, Caruso A, Ferruzza G, Neri R, Rouchy JM, Sprovieri M and Blanc-Valleron MM (2001) Transition from marine to hypersaline conditions in the Messinian Tripoli Formation from the marginal areas of the central Sicilian Basin. *Sedimentary Geology* **140**, 87–105.
- Belmar L, Molina V and Ulloa O (2011) Abundance and phylogenetic identity of archaeoplankton in the permanent oxygen minimum zone of the eastern tropical South Pacific. *FEMS Microbiology Ecology* **78**, 314–26.
- Bernardi E (2013) Integrated stratigraphy of the northernmost record of the Messinian salinity crisis: new insights from the Tertiary Piedmont Basin. PhD thesis, University of Torino, Torino, Italy. Published thesis.
- Bernardi E, Dela Pierre F, Gennari R, Lozar F and Violanti D (2012) Astrochronological calibration and paleoenvironmental reconstruction of the Messinian events at the Northern edge of the Mediterranean: The Govone section (Tertiary Piedmont Basin). *Rendiconti Online Società Geologica Italiana* **20**, 10–11.
- Bigi G, Cosentino D, Parotto M, Sartori R and Scandone P (1990) Structural model of Italy: Geodynamic Project. Consiglio Nazionale delle Ricerche (S.E.L.C.A, scale 1:500,000, sheet 1).
- Birgel D, Guido A, Liu X, Hinrichs K-U, Gier S and Peckmann J (2014) Hypersaline conditions during deposition of the Calcare di Base revealed from archaeological di- and tetraether inventories. *Organic Geochemistry* **77**, 11–21.
- Blanc-Valleron M-M, Pierre C, Caulet JP, Caruso A, Rouchy J-M, Cespuoglio G, Sprovieri R, Pestrea S and Di Stefano E (2002) Sedimentary, stable isotope and micropaleontological records of paleoceanographic change in the Messinian Tripoli Formation (Sicily, Italy). *Palaeogeography, Palaeoclimatology, Palaeoecology* **185**, 255–86.
- Blumenberg M, Mollenhauer G, Zabel M, Reimer A and Thiel V (2010) Decoupling of bio- and geohopanooids in sediments of the Benguela Upwelling System (BUS). *Organic Geochemistry* **41**, 1119–29.
- Blumenberg M, Seifert R, Reitner J, Pape T and Michaelis W (2004) Membrane lipid patterns typify distinct anaerobic methanotrophic consortia. *Proceedings of the National Academy of Sciences* **101**, 11111–16.
- Bond DPG and Wignall PB (2010) Pyrite framboid study of marine Permian-Triassic boundary sections: a complex anoxic event and its relationship to contemporaneous mass extinction. *Bulletin of the Geological Society of America* **122**, 1265–79.
- Bontognali TRR, Vasconcelos C, Warthmann RJ, Bernasconi SM, Dupraz C, Strohmenger CJ and McKenzie JA (2010) Dolomite formation within microbial mats in the coastal sabkha of Abu Dhabi (United Arab Emirates). *Sedimentology* **57**, 824–44.
- Camerlenghi A and Aloisi V (2020) Uncovering the Mediterranean Salt Giant (MEDSALT) - Scientific networking as incubator of cross-disciplinary research in Earth Sciences. *European Review* **28**, 40–61.
- Capella W, Flecker R, Hernández-Molina FJ, Simon D, Meijer PT, Rogerson M, Siero FJ and Krijgsman W (2019) Mediterranean isolation preconditioning the Earth System for late Miocene climate cooling. *Scientific Reports* **9**, article 3795.
- Carnevale G, Gennari R, Lozar F, Natalicchio M, Pellegrino L and Dela Pierre F (2019) Living in a deep desiccated Mediterranean Sea: an overview of the Italian fossil record of the Messinian salinity crisis. *Bollettino della Società Paleontologica Italiana* **58**, 109–40.
- Christeleit EC, Brandon MT and Zhuang G (2015) Evidence for deep-water deposition of abyssal Mediterranean evaporites during the Messinian salinity crisis. *Earth and Planetary Science Letters* **427**, 226–35.
- Cordova-Gonzalez A, Birgel D, Kappler A and Peckmann J (2020) Carbon stable isotope patterns of cyclic terpenoids: a comparison of cultured alkaliphilic aerobic methanotrophic bacteria and methane-seep environments. *Organic Geochemistry* **139**, article 103940.
- Dawson KS, Freeman KH and Macalady JL (2012) Molecular characterization of core lipids from halophilic archaea grown under different salinity conditions. *Organic Geochemistry* **48**, 1–8.
- de Lange GJ and Krijgsman W (2010) Messinian salinity crisis: a novel unifying shallow gypsum/deep dolomite formation mechanism. *Marine Geology* **275**, 273–7.
- De Rosa M and Gambacorta A (1988) The lipids of archaeobacteria. *Progress in Lipid Research* **27**, 153–75.
- Dela Pierre F, Bernardi E, Cavagna S, Clari P, Gennari R, Irace A, Lozar F, Lugli S, Manzi V, Natalicchio M, Roveri M and Violanti D (2011) The record of the Messinian salinity crisis in the Tertiary Piedmont Basin (NW Italy): the Alba section revisited. *Palaeogeography, Palaeoclimatology, Palaeoecology* **310**, 238–55.
- Dela Pierre F, Clari P, Bernardi E, Natalicchio M, Costa E, Cavagna S, Lozar F, Lugli S, Manzi V, Roveri M and Violanti D (2012) Messinian carbonate-rich beds of the Tertiary Piedmont Basin (NW Italy): microbially-mediated products straddling the onset of the salinity crisis. *Palaeogeography, Palaeoclimatology, Palaeoecology* **344–345**, 78–93.
- Dela Pierre F, Clari P, Natalicchio M, Ferrando S, Giustetto R, Lozar F, Lugli S, Manzi V, Roveri M and Violanti D (2014) Flocculent layers and bacterial mats in the mudstone interbeds of the Primary Lower Gypsum unit (Tertiary Piedmont basin, NW Italy): archives of paleoenvironmental changes during the Messinian salinity crisis. *Marine Geology* **355**, 71–87.
- Dela Pierre F, Festa A and Irace A (2007) Interaction of tectonic, sedimentary, and diapiric processes in the origin of chaotic sediments: an example from the Messinian of Torino Hill (Tertiary Piedmont Basin, northwestern Italy). *Bulletin of the Geological Society of America* **119**, 1107–19.
- Dela Pierre F, Natalicchio M, Lozar F, Bonetto S, Carnevale G, Cavagna S, Colombero S, Sabino M and Violanti D (2016) The northernmost record of



- the Messinian salinity crisis (Piedmont basin, Italy). *Geological Field Trips* 8 (2.1), 1–58.
- Eickhoff M, Birgel D, Talbot HM, Peckmann J and Kappler A** (2013) Oxidation of Fe(II) leads to increased C-2 methylation of pentacyclic triterpenoids in the anoxygenic phototrophic bacterium *Rhodospseudomonas palustris* strain TIE-1. *Geobiology* 11, 268–78.
- Elling FJ, Könneke M, Mußmann M, Greve A and Hinrichs K-U** (2015) Influence of temperature, pH, and salinity on membrane lipid composition and TEX<sub>86</sub> of marine planktonic thaumarchaeal isolates. *Geochimica et Cosmochimica Acta* 171, 238–55.
- Elling FJ, Könneke M, Nicol GW, Stieglmeier M, Bayer B, Spieck E, de la Torre JR, Becker KW, Thomm M, Prosser JI, Herndl GJ, Schleper C and Hinrichs K-U** (2017) Chemotaxonomic characterisation of the thaumarchaeal lipidome. *Environmental Microbiology* 19, 2681–700.
- Flecker R, Krijgsman W, Capella W, de Castro Martins C, Dmitrieva E, Mayser JP, Marzocchi A, Modestu S, Ochoa D, Simon D, Tulbure M, van den Berg B, van der Schee M, de Lange G, Ellam R, Govers R, Gutjahr M, Hilgen F, Kouwenhoven T, Lofi J, Meijer P, Sierro FJ, Bachiri N, Barhoun N, Alami AC, Chacon B, Flores JA, Gregory J, Howard J, Lunt D, Ochoa M, Pancost R, Vincent S and Yousfi MZ** (2015) Evolution of the Late Miocene Mediterranean-Atlantic gateways and their impact on regional and global environmental change. *Earth-Science Reviews* 150, 365–92.
- Freeman KH, Hayes JM, Trendel JM and Albrecht P** (1990) Evidence from carbon isotope measurements for diverse origins of sedimentary hydrocarbons. *Nature* 343, 254–6.
- García-Veigas J, Cendón DJ, Gibert L, Lowenstein TK and Artiaga D** (2018) Geochemical indicators in Western Mediterranean Messinian evaporites: implications for the salinity crisis. *Marine Geology* 403, 197–214.
- Gennari R, Lozar F, Natalicchio M, Zanella E, Carnevale G, and Dela Pierre F** (2020). Chronology of the Messinian events in the northernmost part of the Mediterranean: the Govone section (Piedmont Basin, NW Italy). *Rivista Italiana di Paleontologia e Stratigrafia* 126, 517–60.
- Gennari R, Lozar F, Turco E, Dela Pierre F, Lugli S, Manzi V, Natalicchio M, Roveri M, Schreiber BC and Taviani M** (2018) Integrated stratigraphy and paleoceanographic evolution of the pre-evaporitic phase of the Messinian salinity crisis in the Eastern Mediterranean as recorded in the Tokhni section (Cyprus island). *Newsletters on Stratigraphy* 51, 33–55.
- Grothe A, Andreotto F, Reichart G-J, Wolthers M, Van Baak CGC, Vasiliev I, Stoica M, Sangiorgi F, Middelburg JJ, Davies GR and Krijgsman W** (2020) Paratethys pacing of the Messinian Salinity Crisis: low salinity waters contributing to gypsum precipitation? *Earth and Planetary Science Letters* 532, article 116029.
- Han X, Schultz L, Zhang W, Zhu J, Meng F and Geesey GG** (2016) Mineral formation during bacterial sulfate reduction in the presence of different electron donors and carbon sources. *Chemical Geology* 435, 49–59.
- Harvey HR and McManus GB** (1991) Marine ciliates as a widespread source of tetrahymanol and hopan-3 $\beta$ -ol in sediments. *Geochimica et Cosmochimica Acta* 55, 3387–90.
- Hilgen FJ and Krijgsman W** (1999) Cyclostratigraphy and astrochronology of the Tripoli diatomite formation (pre-evaporite Messinian, Sicily, Italy). *Terra Nova* 11, 16–22.
- Hopmans EC, Schouten S, Pancost RD, van der Meer MTJ and Sinninghe Damsté JS** (2000) Analysis of intact tetraether lipids in archaeal cell material and sediments by high performance liquid chromatography/atmospheric pressure chemical ionization mass spectrometry. *Rapid Communications in Mass Spectrometry* 14, 585–9.
- Hsü KJ, Ryan WBF and Cita MB** (1973) Late Miocene desiccation of the Mediterranean. *Nature* 242, 240–4.
- Irace A, Clemente P, Natalicchio M, Ossella L, Trenkwalder S, De Luca DA, Mosca P, Piana F, Polino R and Violanti D** (2009) Geologia e idrostratigrafia profonda della Pianura Padana Occidentale. Firenze: La Nuova Lito, 110 p.
- Irace A, Dela Pierre F and Clari P** (2005) «Normal» and «chaotic» deposits in the Messinian Gessoso-solfifera Fm. at the north-eastern border of the Langhe domain (Tertiary Piedmont basin). *Bollettino della Società Geologica Italiana* 4, 77–85.
- Isaji Y, Kawahata H, Takano Y, Ogawa NO, Kuroda J, Yoshimura T, Lugli S, Manzi V, Roveri M and Ohkouchi N** (2019a) Diazotrophy drives primary production in the organic-rich shales deposited under a stratified environment during the Messinian salinity crisis (Vena Del Gesso, Italy). *Frontiers in Earth Science* 7, article 85.
- Isaji Y, Yoshimura T, Kuroda J, Tamenori Y, Jiménez-Espejo FJ, Lugli S, Manzi V, Roveri M, Kawahata H and Ohkouchi N** (2019b) Biomarker records and mineral compositions of the Messinian halite and K–Mg salts from Sicily. *Progress in Earth and Planetary Science* 6, article 60.
- Jessen GL, Lichtschlag A, Struck U and Boetius A** (2016) Distribution and composition of thiotrophic mats in the hypoxic zone of the Black Sea (150–170 m water depth, Crimea margin). *Frontiers in Microbiology* 7, article 1011.
- Kenig F, Sinninghe Damsté JS, Frewin NL, Hayes JM and De Leeuw JW** (1995) Molecular indicators for palaeoenvironmental change in a Messinian evaporitic sequence (Vena del Gesso, Italy). II: high-resolution variations in abundances and <sup>13</sup>C contents of free and sulphur-bound carbon skeletons in a single marl bed. *Organic Geochemistry* 23, 485–526.
- Kim J-H, van der Meer J, Schouten S, Helmke P, Willmott V, Sangiorgi F, Koç N, Hopmans EC and Sinninghe Damsté JS** (2010) New indices and calibrations derived from the distribution of crenarchaeal isoprenoid tetraether lipids: implications for past sea surface temperature reconstructions. *Geochimica et Cosmochimica Acta* 74, 4639–54.
- Kim ST, Mucci A and Taylor BE** (2007) Phosphoric acid fractionation factors for calcite and aragonite between 25 and 75°C: revisited. *Chemical Geology* 246, 135–46.
- Kleemann G, Poralla K, Englert G, Kjosen H, Liaaen-Jensen S, Neunlist S and Rohmer M** (1990) Tetrahymanol from the phototrophic bacterium *Rhodospseudomonas palustris*: first report of a gammacerane triterpene from a prokaryote. *Journal of General Microbiology* 136, 2551–3.
- Kouwenhoven TJ, Seidenkrantz M-S and van der Zwaan GJ** (1999) Deep-water changes: the near-synchronous disappearance of a group of benthic foraminifera from the Late Miocene Mediterranean. *Palaeogeography, Palaeoclimatology, Palaeoecology* 152, 259–81.
- Krijgsman W, Blanc-Valleron M-M, Flecker R, Hilgen FJ, Kouwenhoven TJ, Merle D, Orszag-Sperber F and Rouchy J-M** (2002) The onset of the Messinian salinity crisis in the Eastern Mediterranean (Pissouri Basin, Cyprus). *Earth and Planetary Science Letters* 194, 299–310.
- Krijgsman W, Capella W, Simon D, Hilgen FJ, Kouwenhoven TJ, Meijer PT, Sierro FJ, Tulbure MA, van den Berg BCJ, van der Schee M and Flecker R** (2018) The Gibraltar Corridor: Watergate of the Messinian Salinity Crisis. *Marine Geology* 403, 238–46.
- Krijgsman W, Fortuin AR, Hilgen FJ and Sierro FJ** (2001) Astrochronology for the Messinian Sorbas basin (SE Spain) and orbital (precessional) forcing for evaporite cyclicity. *Sedimentary Geology* 140, 43–60.
- Kuyppers MMM, Pancost RD, Nijenhuis IA and Sinninghe Damsté JS** (2002) Enhanced productivity led to increased organic carbon burial in the euxinic North Atlantic basin during the late Cenomanian oceanic anoxic event. *Paleoceanography* 17, article 1051.
- Laskar J, Robutel P, Joutel F, Gastineau M, Correia ACM and Levrard B** (2004) A long-term numerical solution for the insolation quantities of the Earth. *Astronomy & Astrophysics* 428, 261–85.
- Lincoln SA, Wai B, Eppley JM, Church MJ, Summons RE and DeLong EF** (2014) Planktonic Euryarchaeota are a significant source of archaeal tetraether lipids in the ocean. *Proceedings of the National Academy of Sciences* 111, 9858–63.
- Löhr SC, Kennedy MJ, George SC, Williamson RJ and Xu H** (2018) Sediment microfabric records mass sedimentation of colonial cyanobacteria and extensive syndepositional metazoan reworking in Pliocene sapropels. *The Depositional Record* 4, 293–317.
- Lozar F, Violanti D, Bernardi E, Dela Pierre F and Natalicchio M** (2018) Identifying the onset of the Messinian salinity crisis: a reassessment of the biochronostratigraphic tools (Piedmont Basin, NW Italy). *Newsletters on Stratigraphy* 51, 11–31.
- Manzi V, Gennari R, Hilgen F, Krijgsman W, Lugli S, Roveri M and Sierro FJ** (2013) Age refinement of the Messinian salinity crisis onset in the Mediterranean. *Terra Nova* 25, 315–22.

- Manzi V, Lugli S, Roveri M, Schreiber BC and Gennari R (2011) The Messinian 'Calcare di Base' (Sicily, Italy) revisited. *Bulletin of the Geological Society of America* **123**, 347–70.
- Manzi V, Roveri M, Gennari R, Bertini A, Biffi U, Giunta S, Iaccarino SM, Lanci L, Lugli S, Negri A, Riva A, Rossi ME and Taviani M (2007) The deep-water counterpart of the Messinian Lower Evaporites in the Apennine foredeep: the Fanantello section (Northern Apennines, Italy). *Palaeogeography, Palaeoclimatology, Palaeoecology* **251**, 470–99.
- Mosca P, Polino R, Rogledi S and Rossi M (2010) New data for the kinematic interpretation of the Alps–Apennines junction (Northwestern Italy). *International Journal of Earth Sciences* **99**, 833–49.
- Natalicchio M, Birgel D, Peckmann J, Lozar F, Carnevale G, Liu X, Hinrichs K-U and Dela Pierre F (2017) An archaeal biomarker record of paleoenvironmental change across the onset of the Messinian salinity crisis in the absence of evaporites (Piedmont Basin, Italy). *Organic Geochemistry* **113**, 242–53.
- Natalicchio M, Dela Pierre F, Birgel D, Brumsack H, Carnevale G, Gennari R, Gier S, Lozar F, Pellegrino L, Sabino M, Schnetger B and Peckmann J (2019) Paleoenvironmental change in a precession-paced succession across the onset of the Messinian salinity crisis: insight from element geochemistry and molecular fossils. *Palaeogeography, Palaeoclimatology, Palaeoecology* **518**, 45–61.
- Natalicchio M, Dela Pierre F, Lugli S, Lowenstein TK, Feiner SJ, Ferrando S, Manzi V, Roveri M and Clari P (2014) Did Late Miocene (Messinian) gypsum precipitate from evaporated marine brines? Insights from the Piedmont Basin (Italy). *Geology* **42**, 179–82.
- Passier HF, Middelburg JJ, de Lange GJ and Böttcher ME (1997) Pyrite contents, microtextures, and sulfur isotopes in relation to formation of the youngest eastern Mediterranean sapropel. *Geology* **25**, 519–22.
- Pearson A and Ingalls AE (2013) Assessing the use of archaeal lipids as marine environmental proxies. *Annual Review of Earth and Planetary Sciences* **41**, 359–84.
- Pettrash DA, Bialik OM, Bontognali TRR, Vasconcelos C, Roberts JA, McKenzie JA and Konhauser KO (2017) Microbially catalyzed dolomite formation: from near-surface to burial. *Earth-Science Reviews* **171**, 558–82.
- Pilskaln CH and Pike J (2001) Formation of Holocene sedimentary laminae in the Black Sea and the role of the benthic flocculent layer. *Paleoceanography* **16**, 1–19.
- Poinsot J, Schneckenburger P, Adam P, Schaeffer P, Trendel JM, Riva A and Albrecht P (1998) Novel polycyclic sulfides derived from regular polyprenoids in sediments: characterization, distribution, and geochemical significance. *Geochimica et Cosmochimica Acta* **62**, 805–14.
- Rashby SE, Sessions AL, Summons RE and Newman DK (2007) Biosynthesis of 2-methylbacteriohopanepolyols by an anoxygenic phototroph. *Proceedings of the National Academy of Sciences* **104**, 15099–104.
- Repeta DJ and Simpson DJ (1991) The distribution and recycling of chlorophyll, bacteriochlorophyll and carotenoids in the Black Sea. *Deep-Sea Research, Part A. Oceanographic Research Papers* **38**, S969–84.
- Repeta DJ, Simpson DJ, Jorgensen BB and Jannasch HW (1989) Evidence for anoxygenic photosynthesis from the distribution of bacterio-chlorophylls in the Black Sea. *Nature* **342**, 69–72.
- Rosenbaum J and Sheppard SMF (1986) An isotopic study of siderites, dolomites and ankerites at high temperatures. *Geochimica et Cosmochimica Acta* **50**, 1147–50.
- Rossi M, Mosca P, Polino R, Rogledi S and Biffi U (2009) New outcrop and subsurface data in the Tertiary Piedmont Basin (NW-Italy): unconformity-bounded stratigraphic units and their relationships with basin-modification phases. *Rivista Italiana di Paleontologia e Stratigrafia* **115**, 305–35.
- Rouchy JM and Caruso A (2006) The Messinian salinity crisis in the Mediterranean basin: a reassessment of the data and an integrated scenario. *Sedimentary Geology* **188**, 35–67.
- Roveri M, Flecker R, Krijgsman W, Lofi J, Lugli S, Manzi V, Sierro FJ, Bertini A, Camerlenghi A, De Lange G, Govers R, Hilgen FJ, Hübscher C, Meijer PT and Stoica M (2014) The Messinian Salinity Crisis: past and future of a great challenge for marine sciences. *Marine Geology* **352**, 25–58.
- Roveri M, Lugli S, Manzi V and Schreiber BC (2008) The Messinian salinity crisis: a sequence-stratigraphic approach. *GeoActa* **1**, 169–90.
- Ryan WBF (2009) Decoding the Mediterranean salinity crisis. *Sedimentology* **56**, 95–136.
- Sabino M, Schefuß E, Natalicchio M, Dela Pierre F, Birgel D, Bortels D, Schnetger B and Peckmann J (2020) Climatic and hydrologic variability in the northern Mediterranean across the onset of the Messinian salinity crisis. *Palaeogeography, Palaeoclimatology, Palaeoecology* **545**, article 109632.
- Santoro AE, Richter RA and Dupont CL (2019) Planktonic marine Archaea. *Annual Review of Marine Science* **11**, 131–58.
- Sanz-Montero ME, Rodríguez-Aranda JP and García Del Cura MA (2008) Dolomite-silica stromatolites in Miocene lacustrine deposits from the Duero Basin, Spain: the role of organotemplates in the precipitation of dolomite. *Sedimentology* **55**, 729–50.
- Schouten S, Hopmans EC, Baas M, Boumann H, Standfest S, Könneke M, Stahl DA and Sinninghe Damsté JS (2008) Intact membrane lipids of 'Candidatus Nitrosopumilus maritimus,' a cultivated representative of the cosmopolitan mesophilic group I Crenarchaeota. *Applied and Environmental Microbiology* **74**, 2433–40.
- Schouten S, Hopmans EC and Sinninghe Damsté JS (2013) The organic geochemistry of glycerol dialkyl glycerol tetraether lipids: a review. *Organic Geochemistry* **54**, 19–61.
- Schouten S, Pavlović D, Sinninghe Damsté JS and de Leeuw JW (1993) Nickel boride: an improved desulphurizing agent for sulphur-rich geomacromolecules in polar and asphaltene fractions. *Organic Geochemistry* **20**, 901–9.
- Schouten S, Villanueva L, Hopmans EC, van der Meer MTJ and Sinninghe Damsté JS (2014) Are Marine Group II Euryarchaeota significant contributors to tetraether lipids in the ocean? *Proceedings of the National Academy of Sciences* **111**, E4285.
- Sharma T and Clayton RN (1965) Measurement of O<sup>18</sup>/O<sup>16</sup> ratios of total oxygen of carbonates. *Geochimica et Cosmochimica Acta* **29**, 1347–53.
- Sierro FJ, Flores JA, Francés G, Vázquez A, Utrilla R, Zamarreño I, Erlenkeuser H and Barcena MA (2003) Orbitally-controlled oscillations in planktic communities and cyclic changes in western Mediterranean hydrography during the Messinian. *Palaeogeography, Palaeoclimatology, Palaeoecology* **190**, 289–316.
- Sierro FJ, Flores JA, Zamarreño I, Vázquez A, Utrilla R, Francés G, Hilgen FJ and Krijgsman W (1999) Messinian pre-evaporite sapropels and precession-induced oscillations in western Mediterranean climate. *Marine Geology* **153**, 137–46.
- Sierro FJ, Hilgen FJ, Krijgsman W and Flores JA (2001) The Abad composite (SE Spain): a Messinian reference section for the Mediterranean and the APTS. *Palaeogeography, Palaeoclimatology, Palaeoecology* **168**, 141–69.
- Simon D and Meijer PT (2017) Salinity stratification of the Mediterranean Sea during the Messinian crisis: a first model analysis. *Earth and Planetary Science Letters* **479**, 366–76.
- Sinninghe Damsté JS and de Leeuw JW (1990) Analysis, structure and geochemical significance of organically bound sulfur in the geosphere. State of the art and future research. *Organic Geochemistry* **16**, 1077–101.
- Sinninghe Damsté JS, Frewin NL, Kenig F and de Leeuw JW (1995a) Molecular indicators for palaeoenvironmental change in a Messinian evaporitic sequence (Vena del Gesso, Italy). I: variations in extractable organic matter of ten cyclically deposited marl beds. *Organic Geochemistry* **23**, 471–83.
- Sinninghe Damsté JS, Kenig F, Koopmans MP, Köster J, Schouten S, Hayes JM and de Leeuw JW (1995b) Evidence for gammacerane as an indicator of water column stratification. *Geochimica et Cosmochimica Acta* **59**, 1895–900.
- Sinninghe Damsté JS, Kuypers MMM, Schouten S, Schulte S and Rullkötter J (2003) The lycopane/C<sub>31</sub> n-alkane ratio as a proxy to assess palaeoacidity during sediment deposition. *Earth and Planetary Science Letters* **209**, 215–26.
- Sinninghe Damsté JS, Schouten S, Hopmans EC, van Duin ACT and Geenevasen JAJ (2002) Crenarchaeol: the characteristic core glycerol dibiphytanyl glycerol tetraether membrane lipid of cosmopolitan pelagic crenarchaeota. *Journal of Lipid Research* **43**, 1641–51.
- Sinninghe Damsté JS, Wakeham SG, Kohnen MEL, Hayes JM and de Leeuw JW (1993) A 6,000-year sedimentary molecular record of chemocline excursions in the Black Sea. *Nature* **362**, 827–9.
- Sollai M, Villanueva L, Hopmans EC, Keil RG and Sinninghe Damsté JS (2019) Archaeal sources of intact membrane lipid biomarkers in the oxygen



- deficient zone of the eastern tropical South Pacific. *Frontiers in Microbiology* **10**, article 765.
- Sturani C** (1973) A fossil eel (*Anguilla* sp.) from the Messinian of Alba (Tertiary Piedmont Basin). Palaeoenvironmental and palaeogeographic implications. In *Messinian Events in the Mediterranean* (ed. C. W. Drooger), pp. 243–55. Amsterdam: Koninklijke Nederlandse Akademie van Wetenschappen.
- Sturani C** (1976) Messinian facies in the Piedmont Basin. *Memorie Società Geologica Italiana* **16**, 11–25.
- Sturani C and Sampò M** (1973) Il Messiniano inferiore in facies diatomitica nel Bacino Terziario Piemontese. *Memorie Società Geologica Italiana* **12**, 335–38.
- Tagliavento M, Lauridsen BW and Stemmerik L** (2020) Episodic dysoxia during Late Cretaceous cyclic chalk-marl deposition – Evidence from framboidal pyrite distribution in the upper Maastrichtian Rørdal Mb., Danish Basin. *Cretaceous Research* **106**, article 104223.
- Teixidor P, Grimait JO, Pueyo JJ and Rodriguez-Valera F** (1993) Isoprenylglycerol diethers in non-alkaline evaporitic environments. *Geochimica et Cosmochimica Acta* **57**, 4479–89.
- Turich C and Freeman KH** (2011) Archaeal lipids record paleosalinity in hypersaline systems. *Organic Geochemistry* **42**, 1147–57.
- Turich C, Freeman KH, Bruns MA, Conte M, Jones AD and Wakeham SG** (2007) Lipids of marine Archaea: patterns and provenance in the water-column and sediments. *Geochimica et Cosmochimica Acta* **71**, 3272–91.
- Van Gernerden H and Mas J** (1995) Ecology of phototrophic sulfur bacteria. In *Anoxygenic Photosynthetic Bacteria* (eds RE Blankenship, MT Madigan and CE Bauer), pp. 49–85. Dordrecht: Springer.
- van Lith Y, Warthmann R, Vasconcelos C and McKenzie JA** (2003) Sulphate-reducing bacteria induce low-temperature Ca-dolomite and high Mg-calcite formation. *Geobiology* **1**, 71–9.
- Vasiliev I, Mezger EM, Lugli S, Reichart GJ, Manzi V and Roveri M** (2017) How dry was the Mediterranean during the Messinian salinity crisis? *Palaeogeography, Palaeoclimatology, Palaeoecology* **471**, 120–33.
- Violanti D, Lozar F, Natalicchio M, Dela Pierre F, Bernardi E, Clari P and Cavagna S** (2013) Stress-tolerant microfossils of a Messinian succession from the Northern Mediterranean basin (Pollenzo section, Piedmont, northwestern Italy). *Bollettino della Società Paleontologica Italiana* **52**, 45–54.
- Wakeham SG, Amann R, Freeman KH, Hopmans EC, Jørgensen BB, Putnam IF, Schouten S, Sinninghe Damsté JS, Talbot HM and Woebken D** (2007) Microbial ecology of the stratified water column of the Black Sea as revealed by a comprehensive biomarker study. *Organic Geochemistry* **38**, 2070–97.
- Wakeham SG, Freeman KH, Pease TK and Hayes JM** (1993) A photoautotrophic source for lycopane in marine water columns. *Geochimica et Cosmochimica Acta* **57**, 159–65.
- Wakeham SG, Sinninghe Damsté JS, Kohnen MEL and de Leeuw JW** (1995) Organic sulfur compounds formed during early diagenesis in Black Sea sediments. *Geochimica et Cosmochimica Acta* **59**, 521–33.
- Wakeham SG, Turich C, Schubotz F, Podlaska A, Li XN, Varela R, Astor Y, Sáenz JP, Rush D, Sinninghe Damsté JS, Summons RE, Scranton MI, Taylor GT and Hinrichs K-U** (2012) Biomarkers, chemistry and microbiology show chemoautotrophy in a multilayer chemocline in the Cariaco Basin. *Deep-Sea Research Part I: Oceanographic Research Papers* **63**, 133–56.
- Warren JK** (2010) Evaporites through time: tectonic, climatic and eustatic controls in marine and nonmarine deposits. *Earth-Science Reviews* **98**, 217–68.
- Warthmann R, van Lith Y, Vasconcelos C, McKenzie JA and Karpoff AM** (2000) Bacterially induced dolomite precipitation in anoxic culture experiments. *Geology* **28**, 1091–4.
- Wilkin RT, Barnes HL and Brantley SL** (1996) The size distribution of framboidal pyrite in modern sediments: an indicator of redox conditions. *Geochimica et Cosmochimica Acta* **60**, 3897–912.
- Zeng Z, Liu X-L, Farley KR, Wei JH, Metcalf WW, Summons RE and Welander PV** (2019) GDGT cyclization proteins identify the dominant archaeal sources of tetraether lipids in the ocean. *Proceedings of the National Academy of Sciences* **116**, 22505–11.